The Journal of Undergraduate Research in Physics

CONTENTS

VOLUME 11, NUMBER 1

DECEMBER, 1991

Published by the Physics Department of Guilford College
for
The American Institute of Physics and The Society of Physics Students

THE JOURNAL OF UNDERGRADUATE RESEARCH IN PHYSICS

This journal is devoted to research work done by undergraduate students in physics and its related fields. It is to be a vehicle for the exchange of ideas and information by undergraduate students. Information for students wishing to submit manuscripts for possible inclusion in the Journal follows.

ELIGIBILITY

The author(s) must have performed all work reported in the paper as an undergraduate student(s). The subject matter of the paper is open to any area of pure or applied physics or physics related field.

SPONSORSHIP

Each paper must be sponsored by a full-time faculty member of the department in which the research was done. A letter from the sponsor, certifying that the work was done by the author as an undergraduate and that the sponsor is willing to be acknowledged at the end of the paper, must accompany the manuscript if it is to be considered for publication.

SUBMISSION

Two copies of the manuscript, the letter from the sponsor and a telephone number where the author can be reached should be sent to:

Dr. Rexford E. Adelberger, Editor
THE JOURNAL OF UNDERGRADUATE
RESEARCH IN PHYSICS
Physics Department
Guilford College
Greensboro, NC 27410

FORM

The manuscript should be typed, double spaced, on 8 1/2 x 11 inch sheets. Margins of about 1.5 inches should be left on the top, sides, and bottom of each page. Papers should be limited to fifteen pages of text in addition to an abstract (not to exceed 250 words) and appropriate drawings, pictures, and tables. Manuscripts may be submitted on a disk that can be read by a MacIntosh™. The files must be compatible with MacWrite™, MicroSoft Word™ or WordPerfect™. Illustrations should be in a MacDraw™ PICT format or TIFF files.

ILLUSTRATIONS

Line drawings should be made with black ink on plain white paper. Each figure or table must be on a separate sheet. Photographs must have a high gloss finish.

CAPTIONS

A brief caption should be provided for each illustration or table, but it should not be part of the figure. The captions should be listed together at the end of the manuscript

EQUATIONS

Equations should appear on separate lines, and may be written in black ink.

FOOTNOTES

Footnotes should be typed, double spaced and grouped together in sequence at the end of the manuscript.

PREPARING A MANUSCRIPT

A more detailed set of instructions for authors wishing to prepare manuscripts for publication in the Journal of Undergraduate Research in Physics can be found in Volume 8 #1 which appeared in October of 1989.

SUBSCRIPTION INFORMATION

The Journal is published twice each academic year, issue # 1 appearing in October and issue # 2 in April of the next year. There are two issues per volume.

TYPE OF SUBSCRIBER	PRICE PER VOLUME
Individual	$US 5.00
Institution	$US 10.00

Foreign subscribers add $US 2.00 for surface postage, $US 10.00 for air freight.

Back issues may be purchased by sending $US 15.00 per volume to the editorial office.

To receive a subscription, send your name, address, and check made out to **The Journal of Undergraduate Research in Physics (JURP)** to the editorial office:

JURP
Physics Department
Guilford College
Greensboro, NC 27410

The **Journal of Undergraduate Research in Physics** is sent to each member of the Society of Physics Students as part of their annual dues.

VOLUME 11 1992-93

The Journal of Undergraduate Research in Physics

Published by the Physics Department
of Guilford College
for

The American Insitute of Physics
and
The Society of Physics Students

ISSN 0731 - 3764

DYNAMICS OF A CHARGED PARTICLE NEAR AN X-TYPE MAGNETIC NEUTRAL POINT

Karen M. Klamczynski *
Physics Department
Illinois State University
Normal, IL 61761
received March 30, 1992

ABSTRACT

We have investigated chaotic motion in a Hamiltonian dynamical system with no dissipation: the neutral line Hamiltonian. In general, both regular (periodic, quasi-periodic, and transient) and chaotic motion are observed in Hamiltonian systems. It had been previously suggested that the Hamiltonian governed by the x^2y^2 potential would exhibit globally chaotic motion (that is, for every set of initial conditions, chaotic motion would result). Dahlqvist and Russberg[1], however, have shown this conjecture to be false by isolating regular motion in several regions of phase space. We propose that the neutral line Hamiltonian, containing the x^2y^2 potential as a special case, will have globally chaotic motion for a wide range of parameter values.

1. P. Dahlqvist and G. Russberg, "Existence of Stable Orbits in the x^2y^2 Potential", Phys. Rev. Lett., 65, 1990, p.2837.

INTRODUCTION

In this investigation of charged particle dynamics near an X-type magnetic neutral point, we were able to address a problem in both pure and applied physics. Chaotic behavior in Hamiltonian systems has been the subject of many research projects. There is much theoretical interest in analytic Hamiltonians that are *globally chaotic*. A globally chaotic system is a system in which every initial condition leads to a chaotic orbit. A candidate for such an analytic Hamiltonian used to be the x^2y^2 potential. Dahlqvist and Russberg[1], however, have isolated a region where regular motion exists in the x^2y^2 potential, thus showing that it is not globally chaotic.

The Hamiltonian for a charged particle in an X-line magnetic field is related to the x^2y^2 potential. However, as a result of the research presented here, this X-line system may be a candidate for a globally chaotic, analytic Hamiltonian.

We define regular motion to include periodic, quasi-periodic and transient behavior. Regular motion has the property of being integrable; that is, the motion, or "orbit," of a particle can be expressed as a known function, an integral, or an infinite series. Regular motion must also be stable. Motion is considered stable if orbits started very close to each other follow similar paths. The simplest kind of regular motion, periodic, is shown in Figure 1-a.

Figure 1-b shows an example of chaotic motion. Unlike regular motion, chaotic motion is neither integrable nor stable. Chaotic motion is characterized by the exponential separation of orbits started very close to each other.

Plotting orbits in real space can be cumbersome, as is evident from Figure 1-b. If the orbit shown were calculated further, it would become increasingly difficult to determine whether the motion being observed were chaotic, quasi-periodic, or transient. In order to facilitate the differentiation between regular and chaotic motion, the Poincaré Surface-of-Section (SOS) technique[2] was used to map motion in x-v_x phase space.

MODEL

The physical model for this research is an X-type magnetic neutral point. An X-type neutral point may be formed when anti-parallel magnetic field lines are pinched together at a point. At the point of contact, the superposition of equal and opposite magnetic fields forms a point of zero net magnetic field, the neutral point. The region around such a neutral point consists of hyperbolic magnetic field lines, as illustrated in Figure 2. Such magnetic structures are often modeled in space plasmas, e.g. in the Earth's magnetic tail[3]. The magnetic field in Figure 2 is given by:

The author participated in this research project while an undergraduate at Illinois State University. In August, 1992, she graduated cum laude with honors in physics. She is currently a graduate student in the Space Physics and Astronomy Department at Rice University in Houston, Texas

$$B = B_{xo}\frac{y}{T}\hat{e}_x + B_{yo}\frac{x\sqrt{\delta}}{T}\hat{e}_y \ , \qquad (1)$$

where B_{xo} and B_{yo} are the components of the magnetic field at the point $y = T$ and $x = T/\delta^{1/2}$; T is an arbitrary length scale, and $\hat{e}_x$ and $\hat{e}_y$ are orthogonal unit vectors in the x-y plane. The parameter δ is related to the angle θ in Figure 2 by the relation $\delta^{1/2} = \tan\theta$.

The equations of motion for a single charged particle in this system may be easily obtained by using the Lorentz Force law and Newton's Second Law:

$$\frac{d^2x}{dt^2} = \frac{\Omega_{xo}}{T}[\delta x v_z] \qquad (2a)$$

$$\frac{d^2y}{dt^2} = -\frac{\Omega_{xo}}{T}[\delta y v_z] \qquad (2b)$$

$$\frac{d^2z}{dt^2} = \frac{\Omega_{xo}}{T}[y v_y - \delta x v_x] \ , \qquad (2c)$$

where

$$\frac{\Omega_{xo}}{T} = \frac{q\,B_{xo}}{m}$$

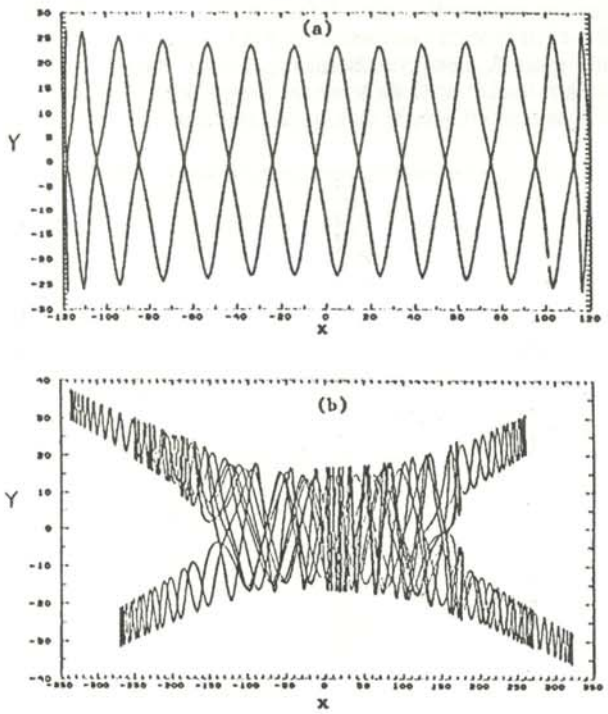

Figure 1

(a) Example of a regular orbit. Note that this orbit is periodic.

(b) Example of a chaotic orbit.

is a gyrofrequency: the angular frequency of motion about a uniform magnetic field of magnitude B_{xo}.

Of Equations (2), only Equation (2c) can be directly integrated. The result of this integration is:

$$\frac{dz}{dt} = \frac{\Omega_{xo}}{2T}[y^2 - \delta x^2] + v_{zo} \ . \qquad (3)$$

Using this result in equations (2a) and (2b), we find two coupled differential equations which can be numerically solved:

$$\frac{d^2x}{dt^2} = \frac{\Omega_{xo}\,\delta x}{T}\left[\frac{\Omega_{xo}}{2T}(y^2 - \delta^2 x^2) + v_{zo}\right] \qquad (4a)$$

$$\frac{d^2y}{dt^2} = \frac{\Omega_{xo}\,y}{T}\left[\frac{\Omega_{xo}}{2T}(y^2 - \delta^2 x^2)\right] \ . \qquad (4b)$$

At this point, it was convenient to switch to the rotated coordinate system of Dahlqvist and Russberg (henceforth referred to as DR). Here, the x-axis is rotated through the angle $\theta = \tan^{-1}(\delta^{1/2})$; the result of this rotation is to align the x-axis along one of the field line asymptotes. In this coordinate system, the equations of motion are as follows (when v_{zo} is taken to be zero):

$$\frac{d^2x}{dt^2} = -\frac{\Omega_{xo}^2\sqrt{\delta}}{2T^2}[2\sqrt{\delta}\,x\,y^2 + (1-\delta)\,y^3] \qquad (5a)$$

$$\frac{d^2y}{dt^2} = -\frac{\Omega_{xo}^2}{2T^2}[2\,\delta\,x^2\,y + 2\sqrt{\delta}\,(1-\delta)x\,y^2 + (1-\delta)^2\,y^3] \ . \qquad (5b)$$

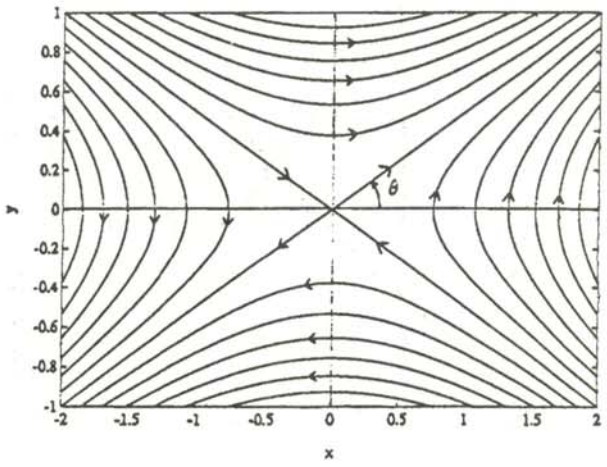

Figure 2

An "X-type" magnetic neutral point. The field lines around the neutral point are hyperbolic. The contour plot of the effective potential function for a charged particle will have the same shape.

We can write the Hamiltonian in the rotated coordinate system as:

$$H = \frac{1}{2} m (v_x^2 + v_y^2) + V(x,y) \quad , \tag{6}$$

where

$$V(x,y) = \frac{\Omega_{xo}^2}{8 T^2} [2 \sqrt{\delta}\ x\ y + (1 - \delta)\ y^2]^2 \tag{7}$$

is an effective potential. Note that this potential reduces to the x^2y^2 potential when $\delta = 1$ (i.e. when the asymptotes of the magnetic field lines are perpendicular). Equations (5) were numerically integrated on an IBM RS/6000 computer, and the resulting particle trajectory data were analyzed.

RESULTS

A reproduction of the DR periodic orbit is shown in Figure 3-a. This figure shows the trajectory of a particle in the x-y plane; the particle exhibits periodic motion.

When the angle θ is decreased from 45 degrees to 44.9 degrees, the motion of a particle started with the same initial conditions is observed to be chaotic, as shown in Figure 3-b. This shows that a slight perturbation of the potential function can result in a transition from a regular orbit to a chaotic orbit. We examine the effects of decreasing the parameter δ from $\delta = 1$ (High δ), which are perturbations of the DR system, as well as the case of increasing δ from zero (Low δ).

HIGH δ

Figure 4-a shows a reproduction of the DR region using the Poincaré Surface-of-Section (SOS) technique. The rest of the parts of Figure 4 show the results of perturbing this system. As the parameter δ is decreased from $\delta = 1$ to $\delta = .9999$ (a change of $\theta = .0029$ degrees), the shape of the DR region, shown in Figure 4-b, changes slightly. In addition, four small regions appear which were not observed at $\delta = 1$ (These can be observed upon magnification). Further decreasing δ to $\delta = .99987$, Figure 4-c, reveals that the original DR region shows signs of an impending bifurcation, while the four small peripheral regions coalesce into two regions, which are barely visible in the dark areas near the DR region.

The original DR region bifurcates completely, as seen in figure 4-d, by $\delta = .99983$. No further bifurcations of this region were observed, and beyond $\delta = .99983$, Figures 4-e and 4-f, the region appears to shrink until no regular motion is observed. The total perturbation required to destroy the DR region is .0054 degrees; that is, decreasing θ from 45 degrees to 44.9946 degrees apparently causes the original DR region to disappear.

On the other hand, we have observed that the peripheral regions undergo interesting size and shape changes. By following the series of plots in Figure 4, we can see that the peripheral regions appear to grow in size until Figure 4-d ($\delta = .9998225$). This is partially true, at $\delta = .99986$, the regions abruptly become larger; then they again shrink in size by $\delta = .99985$. (For the sake of space, this is not shown in Figure 4.) During this period where the regions alternately grow and shrink in size, the regular outer orbits also change in shape to a higher or lower degree of symmetry. In the last three plots shown in Figure 4, these peripheral regions are shown to decrease in size until they are no longer seen in Figure 4-f. These regions are, in fact, quite complex. Enlargements

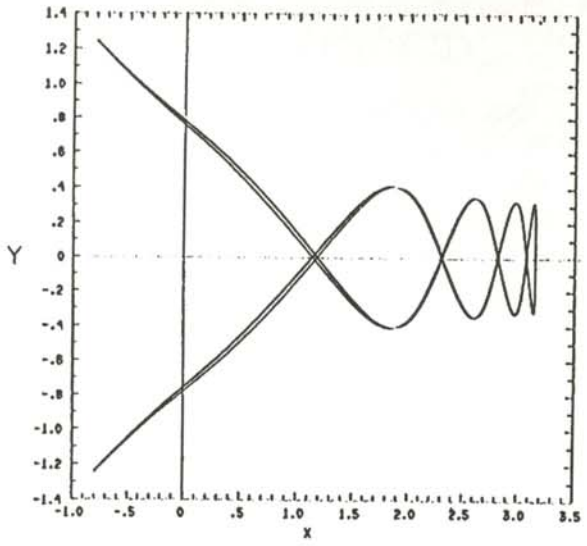

Figure 3(a)
A reproduction of a Dahlqvist and Russberg regular orbit ($\delta = 1$), shown in the x-y plane.

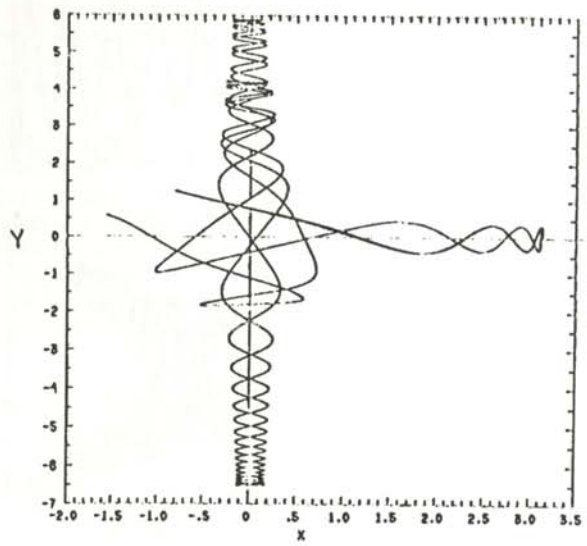

Figure 3(b)
A reproduction of a Dahlqvist and Russberg orbit, starting with the same initial conditions as Figure 3(a), having a value of the parameter $\delta = .997$. This yields a chaotic orbit.

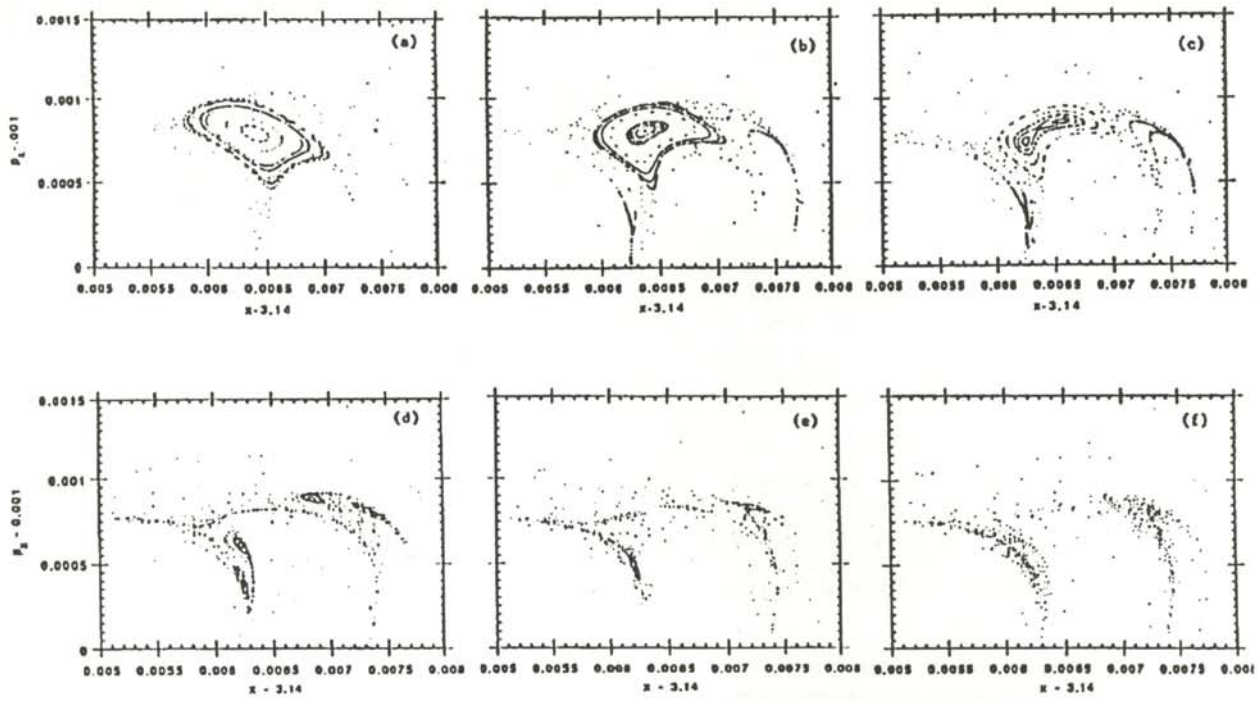

Figure 4

Series of Surface-of-Section (SOS) plots from our High δ results. All of the plots are centered around the same region. (a) δ = 1 (reproduction of Dahlqvist and Russberg regular region; (b) δ = .9999; (c) δ = .99987; (d) δ = .99983; (e) δ = .99981; (f) δ = .99980.

of these regions confirm that as the regions decrease in size, the outer quasi-periodic orbits break up into chains of quasi-periodic orbits, known as islands.

These peripheral regions, which shrink until no regular motion is observed to the precision of our calculations, are not observed at δ = .99980665; this value of δ corresponds to a total potential perturbation of θ = .0055 degrees. Martin and Matsuoka[4] have argued that the regular regions actually disappear (as opposed to continually shrinking and bifurcating) as a result of their extrapolation of the relation between the size of the region and the corresponding value of δ.

LOW δ

When δ = 0, or θ = 0 degrees, the system is modeled by anti-parallel magnetic field lines. This system is regular, that is, every set of initial conditions results in regular motion. As δ is increased, regular motion becomes restricted to finite regions, with chaotic motion elsewhere. This situation is shown in Figure 5.[5] Similar to the High δ results, we observe in Figure 5 that further changing δ results in the shrinking of regions of regular motion. By δ = .2576864 (θ = 14.45 degrees), regular motion is no longer observed.

In contrast to the High δ investigation, increasing δ from δ = 0 to δ = .2576864 results in numerous, repeated bifurcations. Figure 6 shows one particular series of bifurcations. In Figure 6-a, we see a region of regular motion with two points of stability. As δ is increased, this region splits into two regions, shown in Figure 6-b.

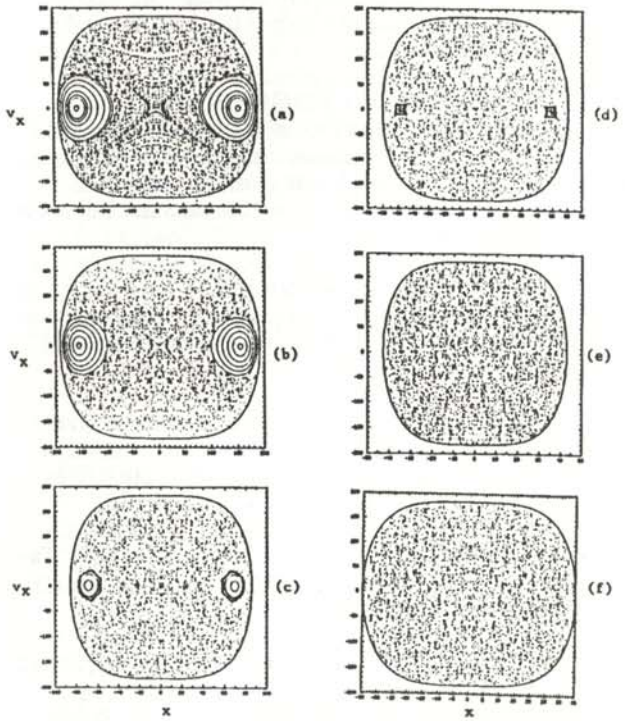

Figure 5

A series of SOS plots for low δ results. All the plots are centered around the same region. (a) δ = .0025; (b) δ = .01; (c) δ = .05; (d) δ = .1; (e) δ = .2; (f) δ = .3.

Finally, as we further increase δ, Figure 6-c shows that this region repeatedly splits into progressively smaller regular regions. Upon magnifying the small regular regions in 7-c, we have observed that the region in this figure contains very many tiny regular regions.

CONCLUSIONS

Our study has shown that changing the angle between the asymptotes of the X-type magnetic field, thereby destroying its symmetry, results in the apparent demise of regular motion. For the High δ case, it appears that varying the potential function from the highly symmetric x^2y^2 causes the regular motion which was observed by DR to disappear; this was observed after altering the angle θ from 45 degrees to 44.9946 degrees. Also, as θ was decreased further, to 44.9945 degrees, no other regular motion was observed.

As a result of our investigation at Low δ, we observed restricted areas of regular motion for values of δ near zero. As we increased δ, these regular regions repeatedly split into smaller regular regions, until no regular motion is observed at δ = .2576864; this value of δ corresponds to the angle θ = 14.45 degrees.

We have observed no regular motion in the interval .2576864 < δ < .99980665. Hence, this region may define a set of systems whose Hamiltonians are globally chaotic.

Finally, this system is of interest physically to physicists interested in studying the magnetosphere of the earth, particularly those studying the Magnetic Reconnection theory and behavior of charged particles in the distant magnetic tail.

ACKNOWLEDGEMENTS

The author would like to especially thank Dr. Richard F. Martin, Jr., for valuable guidance and patience throughout this project. This work was partially supported by NSF grant ATM-9002447 and an Illinois State University Research Grant.

REFERENCES

* Present address of author: Department of Space Physics and Astronomy, Rice University, PO Box 1892, Houston, TX 77251-1892.

1. P. Dahlqvist and G. Russberg, "Existence of Stable Orbits in the x^2y^2 Potential," Physical Review Letters, 65, 1990, p. 2837. This paper also cites references to previous work on the x^2y^2 potential.

2. For an explanation of this technique, see e.g. M. Tabor, Chaos and Integrability in Nonlinear Dynamics, John Wiley, NY, 1989, p. 118.

3. R.F. Martin and T.W. Speiser, "Nonlinear Dynamics of the Neutral Line Hamiltonian," in Physics of Space Plasmas (1991), SPI Conference Proceedings and Reprint Series, Number 11, G.B. Crew and J.R. Jasperse, eds., Scientific Publishers, Inc., Cambridge, MA, 1992, pp 311-334.

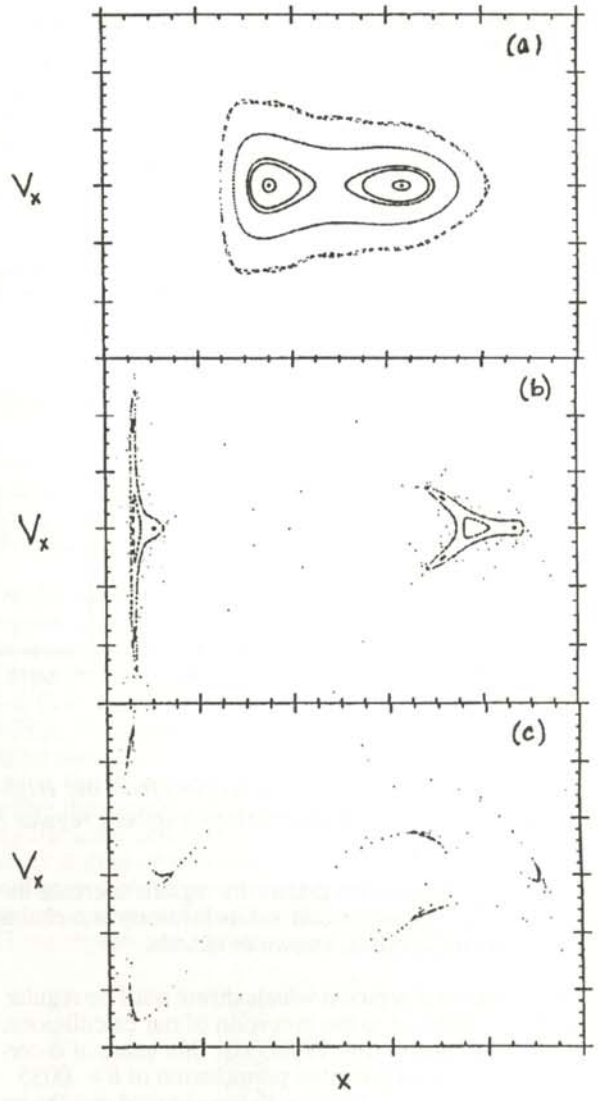

Figure 6
Enlargement of a region with regular motion for different values of δ.
(a) δ = .255; (b) δ = .2575; (c) δ = .2576863.

4. R.F. Martin, Jr. and H. Matsuoka, "Large Scale Chaos in the Neutral Line Hamiltonian", Phys. Rev. A, in press, 1992.

5. G.R. Burkhart, R.F. Martin, Jr., P.B. Dusenbery, and T.W. Speiser, "Neutral Line Chaos and Phase Space Structure," Geophys. Res. Letters, 18, 1591-1594, 1991.

FACULTY SPONSOR

Dr. Richard F. Martin, Jr.
Physics Department
Illinois State University
Normal, IL 61761-6901
309-438-5382
rfm@entropy.phy.ilstu.edu

'IN-SITU' SURFACE ENHANCED RAMAN SPECTRO-ELECTROCHEMICAL STUDIES OF THE SURFACE FILMS ON NICKEL IN AN AQUEOUS SOLUTION ENVIRONMENT †

Mark Pankuch
Illinois Benedictine College
Lisle, IL 60532
Received November 7, 1991

ABSTRACT

Laser Raman Spectroscopy was used to identify 'in-situ' the passive films on nickel. We used surface enhanced Raman Scattering by the electrochemical deposition of silver on the nickel electrode. The electrolytes studied were solutions of NaCl and NaOH. We found a correlation between the cyclic voltammogram and the formation of different surface species. We identified both $Ni(OH)_2$ and NiO films. These films were produced independently. We also identified absorbed Cl^- in the NaCl solutions.

INTRODUCTION

During the oxidation of nickel, various thin surface films are produced. These films form a passive layer over the nickel, protecting it from further corrosion or pitting. There is interest in these films due to the extensive practical uses of nickel. Although many different techniques have been used to examine these films, there still is a debate on the composition of the surface films. Some have proposed that the passive film is $Ni(OH)_2$ [1-4] while others believe it to be NiO [5-7].

This lack of consensus is partially due to the lack of a technique sensitive enough to identify surface films a few atomic layers thick. In this work, Laser Raman Spectroscopy (LRS) in combination with cyclic voltammery was used to study the oxidation of nickel. Laser Raman Spectroscopy is a technique where light of a known frequency is scattered off a sample. Most of the light which hits the molecules of the sample is elastically scattered in all direction. However, a small fraction of the light will scatter inelastically, changing the molecule's vibrational or rotational energy state. To make this transition, energy must be absorbed or given off by the incident photon. This change in photon energy corresponds to a shift in the frequency of the light which is known as the Raman effect. Using a spectrometer, one can generate a plot of scattered light intensity vs frequency shift (given in wave numbers). Since every molecule rotates and vibrates differently, the spectrum will show unique bands, characteristic of each substance, and therefore is an excellent analytical device.

Mark is a senior at Illinois Benedictine College in Lisle, Illinois. He is majoring in physics with a minor in mathematics. The present work was done at Argonne National Laboratory under the Science and Engineering Research Semester program, sponsored by the Department of Energy. After graduation, he plans to obtain a Ph.D. in physics or in a closely related field.

Cyclic voltammery is an electrochemical technique that measures electrochemical current as a function of an applied potential. Imagine a pure nickel surface in solution. As a more and more positive potential is applied to the metal, (ie. an anodic scan) the metal's electrons become attracted and eventually, at a certain potential, will be pulled off. A situation such as:

$$Ni \rightarrow Ni^{2+} + 2e^-$$

will occur. This flow of electrons is actually a rise in the current that shows up as a peak in a cyclic voltammogram. The oxidized metal, in the form of a Ni^{2+} ion, can now form an oxide or hydroxide complex on the surface. Voltammogram peaks indicate that surface film are being formed, but tell nothing of their actual makeup. If the film dies not dissolve in solution, it creates a passive film that prevents further corrosion. This whole process can be reversed by sweeping the potential negative (cathodically) to reduce the oxidized film back to pure metal.

These two techniques work very well together. Cyclic voltammery is used to find at what potential things are

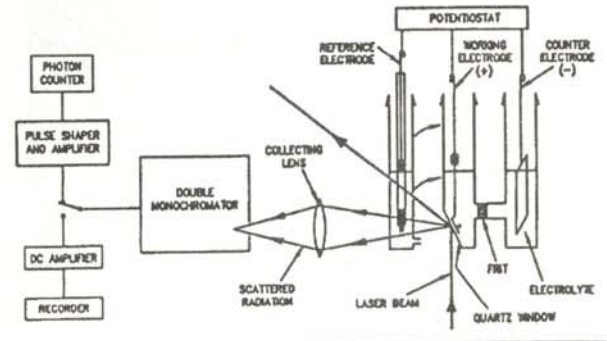

Figure 1
Experimental set-up for laser Raman spectro-electrochmistry.

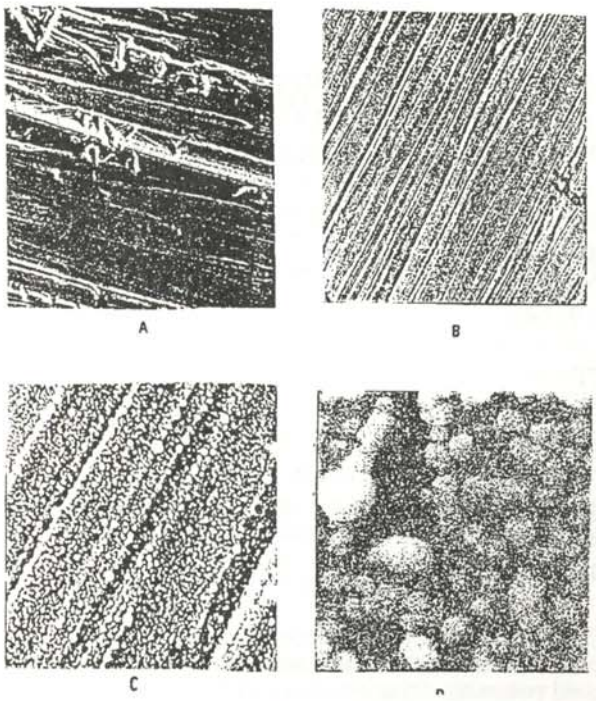

Figure 2
Scanning Electron Miscroscope photosgraphs of the nickel electrode surface. A) Clean nickel, no silver deposited, x 1000. The other photos are with silver deposited :B) x 1000, C) x 6000, and D) x 54,000

happening. Raman spectroscopy tells us what is actually present.

LRS had been attempted earlier to identify the composition[8], but the spectrum was too weak. Since then, the new method of surface enhanced Raman scattering (SERS) was discovered. [9,10] In SERS, metals of gold, copper or silver are used to greatly enhance the Raman scattering. Nickel, deposited onto silver, has been used in the past [9,10], but in our work, silver was electrochemically deposited on to a nickel electrode.

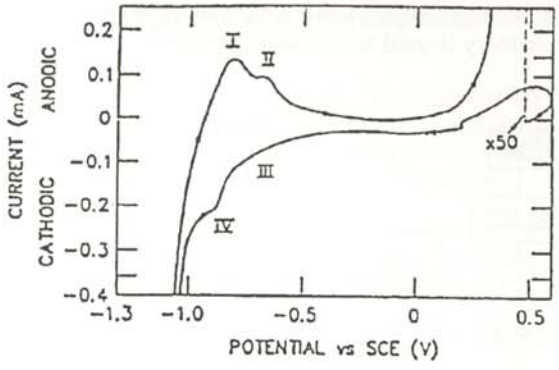

Figure 3
Cyclic voltammogram of nickel in 0.15M NaCl solution (pH 8.5). The scan rate was 10 mV/sec. The regions indicated by Roman numerals indicate the presence of different surface species.

THE EXPERIMENT

The nickel electrodes were made of high purity material (99.9%), cut into sheets about 3 mm in width. The electrodes were polished with 600 grit emery paper, cleaned with acetone and then rinsed with distilled water. The electrodes were cleaned cathodically by a 15 minute polarization at -1.3V. The electrode was then removed from the cell and silver was deposited in a 1mM $AgNO_3$/1mM HNO_3 solution. A potential of 0.0V with respect to a saturated calomel reference electrode (SCE) was applied to deposit from 10 to 15 mC/cm^2 of charge.

After the silver deposition, the nickel electrode was placed back in the electrolyte solution and again cleaned at -1.3V for 15 to 30 minutes. This process assured us a clean nickel surface, free from any surface films formed by exposure to the air during transfer between cells.

The Raman spectroscopy was done in a three chambered spectro-electro-chemical cell made of quartz, shown in Figure 1. The sample chamber had a quartz window, tilted at 60 degrees from the horizontal for accepting the laser beam. A platinum counter electrode was used along with a SCE for reference. The nickel electrode was then linearly raised at 5 mV/sec to more positive values for Raman spectral measurements.

To be sure that the enhancing electrodeposited silver did not completely cover the nickel surface, a scanning electron microscope (SEM) was used to obtain images of the surface. Figure 2 shows such a picture. The silver forms various islands, ranging in size from 55 to 350 nm. Surface films of the nickel formed between these islands give much stronger Raman bands which can be easily detected.

RESULTS

USING A NaCl SOLUTION

A typical cyclic voltammogram of nickel in NaCl solution (pH 8.5) is shown in Figure 3. Two anodic waves

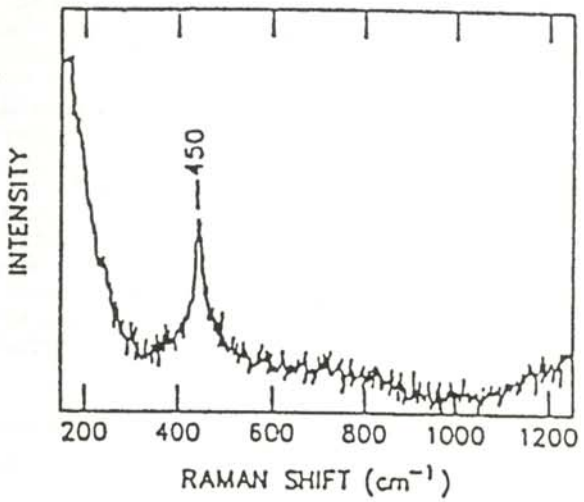

Figure 4
Surface enhanced Raman spectrum of corrosion film on nickel in 0.15M NaCl at E = -0.75 V vs. SCE. We used the 514.5 nm line of a 100 mW Ar+ laser.

(marked I and II in the Figure 2) are clearly shown. Since the oxidation of nickel is reversible, we expect an equal number of cathodic waves. These are also present and marked in Figure 2 as III and IV. The combination of these waves would occasionally differ in their relative sizes, but were always reproduceable.

Raman signals appear after the first anodic wave of the cyclic voltammogram around a potential of -0.75V. Figures 4 and 5 show the Raman spectrum using the 514.4 nm line from a 100 mW Ar^+ laser. There is a sharp band at 450 cm^{-1} seen in Figure 4 and a shoulder at 3640 cm^{-1} on the bulk water band at 3500 cm^{-1} seen in Figure 4. The 450cm^{-1} band has been identified as the stretching mode of Ni-OH [9,10], allowing us to deduce the presence of $Ni(OH)_2$. The 3640 cm^{-1} band is assigned to the hydroxide group, giving further evidence that $Ni(OH)_2$ is present.

Figure 6 shows the Raman spectrum that is observed when the electrode potential is taken past the second peak indicating the presence of another surface species. A new band at 510 cm^{-1} is now present which is quite broad and appears as a distinct shoulder of the 450 cm^{-1} band. This band has been assigned to NiO. The appearance of another band at 215 cm^{-1} is the second most noticeable change. The band appears only at more positive potentials and seems to shift to higher frequencies with higher potential. For these reasons and comparison with other works [11,12], the band is attributed to absorbed Cl^- ions on the silver surface.

The general features of the spectrum shown in Figure 6 do not change for potentials up to 0.0V. When the voltage is taken past this region, the deposited silver oxidizes, eliminating the SERS spectrum. If the potential is brought to -1.3V, the reduction of the passive nickel

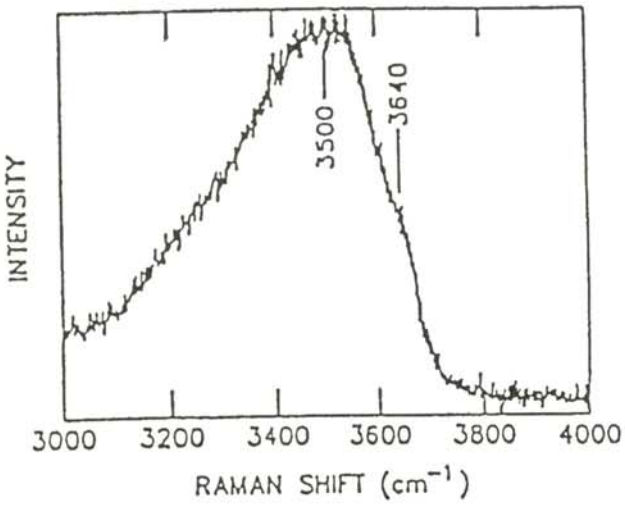

Figure 5
Surface enhanced Raman spectrum of corrosion film on nickel at -0.75V in the region of OH stretching. The peak at 3500 cm^{-1} is from bulk water. The sholder at 3640 cm^{-1} is the O-H stretching mode of the hydroxide group.

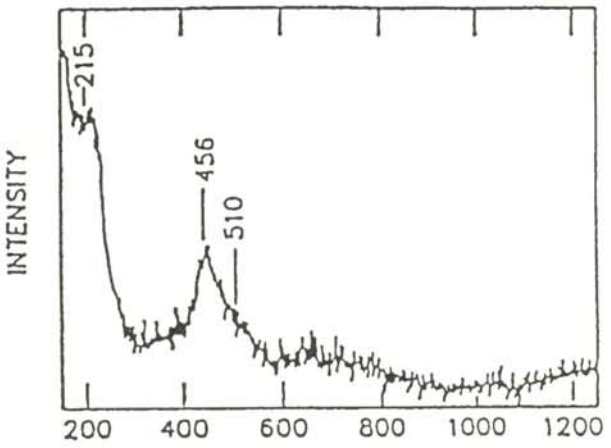

Figure 6
Surface enhanced Raman spectrum of corrosion film on nickel at -0.4 V showing the new band at 510 cm^{-1}. This band is assigned to NiO.

film occurs, leaving two very weak bands and 450cm^{-1} and 510cm^{-1}. The presence of these bands suggests that the kinetics of reduction are rather slow.

We performed similar experiments with the electrode in a NaCl solution with a pH of 2.7 which yielded nearly identical results, see Figure 7. We were able to identify Ni(OH)2 bands, but could not get spectra past the second peak because this peak appears after the oxidation of silver.

USING A NaOH SOLUTION

Our results with the electrode in a 0.1M NaOH solution are much like those already presented. The voltammogram of the nickel closely resembles that shown in Figure 3, but the anodic peaks appear at a slightly lower potential. The spectrum of the film at a potential just

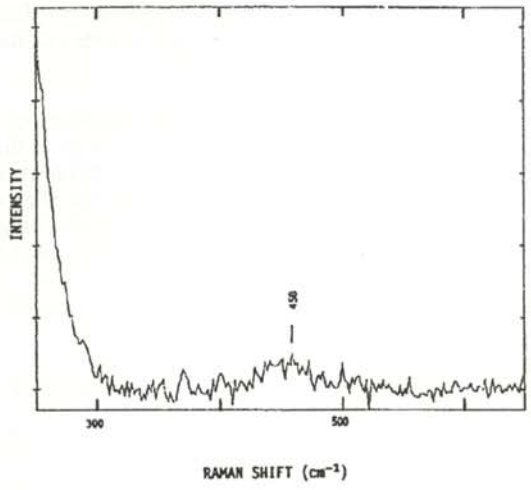

Figure 6
Surface enhanced Raman spectrum of corrosion film on nickel in acidified NaCl solution (ph 2.7) at 0.0V. The band at 458 cm^{-1} indicates the presence of $Ni(OH)_2$.

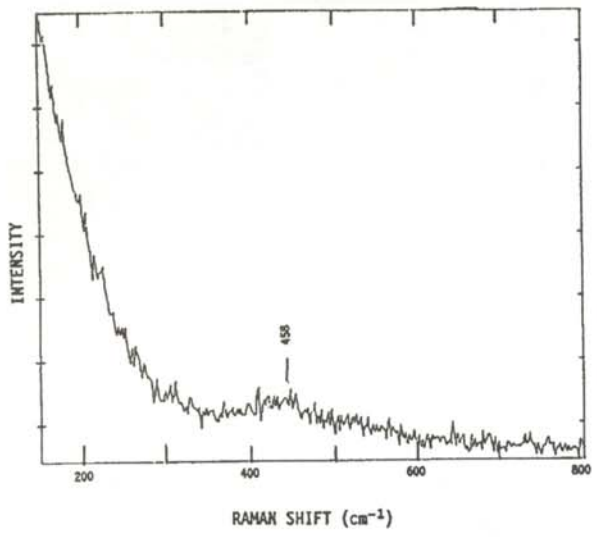

Figure 8
Surface enhanced Raman spectrum of the surface film formed on nickel in 0.1M NaOH at -0.8V. The band at 458 cm-1 indicates the presence of Ni(OH)2.

past the first peak (≈ -0.8V) is shown in Figure 8. A band, although somewhat weak and broad, is present around 450 cm^{-1}, signifying the presence of $Ni(OH)_2$. From scans to higher frequencies we again noted the band positioned at 3640cm^{-1}. These bands grew more intense at higher potentials corresponding to thickening of the surface film.

Scans past the second wave (-0.6V) also show the band at 510 cm^{-1}. In this region, the 450 cm^{-1} band is much more intense and defined. The 510 cm^{-1} band often appears as a shoulder, but occasionally, two clear peaks can be seen as shown in Figure 9. It should be noted that no signal around 218 cm^{-1} is formed in the NaOH solutions as it was in the NaCl solution. This supports our theory that this band was due to absorbed Cl^-.

The oxidation/reduction potential of the deposited silver in NaOH is around +0.25V. Raman spectra up to this potential gave similar results to those obtained immediately past the second wave, but they do become sharper and more intense. We interpreted this as a thickening of the passive film. Attempts to reduce the film were relatively successful, but two very weak bands and 450 cm^{-1} and 510 cm^{-1} remained, even at potentials as negative as -0.9V, again indicating slow reduction kinetics.

In both NaCl and NaOH, a similar yet unpredicted effect was found when the potentials of the cyclic voltammogram were scanned past the oxidation potential of silver and then immediately reversed. Sharpening of the 450 cm^{-1} band and a new band at 3570 cm^{-1} would appear with a strong amplification of the 3640 cm^{-1} band. These effects might be a consequence of a conversion of the crystal structure of alpha $Ni(OH)_2$ to beta $Ni(OH)_2$ (the sharpening at 450 cm^{-1}) and absorption of water (the new band at 3570 cm^{-1}). This voltage scanning process should cause a fraction of the silver to be dissolved and then immediately redeposited. During the redeposition of the silver, laser light was incident on the nickel. It has been previously seen that laser illumination during oxidation/reduction of silver results in a further magnification of the SERS[13].

Our results correlate for the first time the SERS of the surface films on nickel to the anodic waves of the cyclic voltammogram. We find that the first anodic wave corresponds to the formation of $Ni(OH)_2$. The second anodic peak is due to the formation of NiO on the metal surface. We showed that the NiO is produced independently and not as a conversion of $Ni(OH)_2$ by dehydration as others have suggested. [1,14]

ACKNOWLEDGMENTS

The author would like to thank the Division of Educational Programs at Argonne for the opportunity to undertake this research. Thanks are due to Mr. Ben Tani for his instructions in taking the SEM photographs. An extra special thanks goes to my advisor, Dr. Carlos A. Melendres, for his generous guidance, instructions, patience and friendship.

REFERENCES

† This work was sponsored by the Department of Energy through the Student Research Participation Program at Argonne National Laboratory.

1. W. Paik and Z. Szklarska-Smialowska, Surface Science, 96, 1980, p. 401.

2. R.E. Hummel, R.J. Smith and E.D. Verink, Jr., Corrosion Science, 27, 1987, p. 803.

3. R. J. Smith, R.E. Hummel and J.R. Ambrose, Corrosion Science, 27, 1987, p. 815.

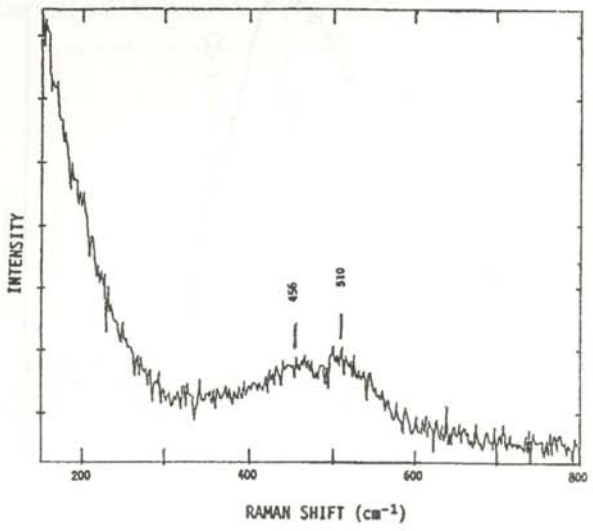

Figure 9
Surface enhanced Raman spectrum of the surface film formed on nickel in 0.1M NaOH at -0.6V. The lack of a band around 218cm-1 indicates that no Cl^- is present.

4. D.J. Kim and W. Paik, J. of the Korean Chemical Society, 26, 1982, p. 369.

5. W. Visscher, Journal de Physique, 44, C10, 1983, p. 213.

6. B. MacDougall and M. Cohen, J. Electrochem. Socl, 123, 1976, p. 191.

7. W. Visscher and E. Barendrecht, Surface Science, 135, 1983, p. 436.

8. C.A. Melendres and S. Xu, J. Electrochem. Soc., 131, 1984, p. 2239.

9. J. Desilvestro, D.A. Corrigan and J.J. Weaver, J. of Phys. Chem., 90, 1986, p. 6408.

10. J. Desilvestro, D.A. Corrigan and M.J. Weaver, J. Electrochem. Soc., 135, 1988, p. 885.

11. D.Roy and T.E. Furtak, Chem. Phys. Let., 129, 1986, p. 501.

12. B. Pettinger, M.R. Philpott and J.G. Gordan, J. Chem. Phys., 74, 1981, p. 934.

13. S.H. Macomber, T.E. Furtak and T.M. Devine, Chem Phys. Lett., 90, 1982, p. 439.

14. J.O.M. Bockris, A.K.N. Reddy and B. Rao, J. Electrochem. Soc., 113, 1966, p.113

FACULTY SPONSOR

Dr. Carlos A. Melendres
Materials Science and Chemical Technology Divisons
Argonne National Laboratory
9700 South Cass Avenue
Argonne, IL 60439-4837

DESIGN AND PERFORMANCE OF A COMPUTER-CONTROLLED DATA SYSTEM FOR EMISSION SPECTROPHOTOMETERS

M.E. Ciholas *
Department of Physics
Centre College
Danville, KY 40422
received 1/22/92

ABSTRACT

This paper describes the design and performance of a computer-controlled data system for emission spectrophotometers. The core of the system is an interface and software for an enhanced Apple IIe microcomputer. The system controls the spectrophotometer stepper motor and stores and processes the photomultiplier output. Digital smoothing, deconvolution, baseline adjustment, and video and plotter display of the spectra are available. The novel features of our work are low cost and relatively high performance from from a microprocessor with limited capability. The system performance is illustrated with typical spectra.

INTRODUCTION

Computer control of spectrophotometers has existed for some time, as have digital processing and enhancement of spectral data. Reviews of the field can be found in the literature. [1-3] Microcomputer interfaces have been designed to characterize the output of pulsed hollow cathode lamps for atomic absorption spectroscopy. [4] An approach, which in some ways parallels that reported by us, for an interface for EPR spectrometer control and data acquisitions has been reported in the literature.[5]

Our data station uses an enhanced Apple IIe microcomputer interfaced to a spectrometer with a photomultiplier detector and signal amplifier attached. [6] With some modification, our approach should be applicable to most emission spectrometers with stepper-motor control of grating rotation and a detector signal that can be amplified to the 0 - 1 Volt range.

The advantages of our data system over those available commercially include much lower cost, user flexibility and some features not generally available (e.g. deconvolution). A significant investment in software is required.

Our system controls the spectrophotometer's stepper motor and amplifies, stores, displays, plots and processes the signal from the spectrophotometer. The system performance is illustrated with the Zeeman spectra of Hg. The wavelength separation of the Zeeman components can easily be controlled. This approach provides a convenient means of testing instrumental resolution and the effects of digital smoothing and deconvolution of the spectral data.

HARDWARE

Figure 1 shows an overview of our system. The mini-step driver, supplied with the spectrophotometer, supplies the pulses to the phase windings of the grating stepper motor. Four TTL signals are needed to control the driver: a direction bit controlling forward or reverse; a

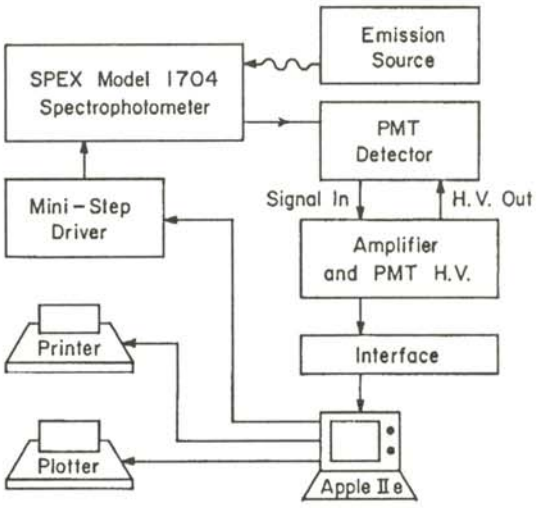

Figure 1
System components for the computer-controlled emission spectrophotometer

The author received his B.Sc. from Centre College in 1986 with a major in Physics and minors in Mathematics and Computer Science. He received his M.Sc. degree in Electrical Engineering and Computer Science from MIT in 1988. He is currently employed as a research engineer at MIT in the Advanced Network Architecture group of the Laboratory for Computer Science.

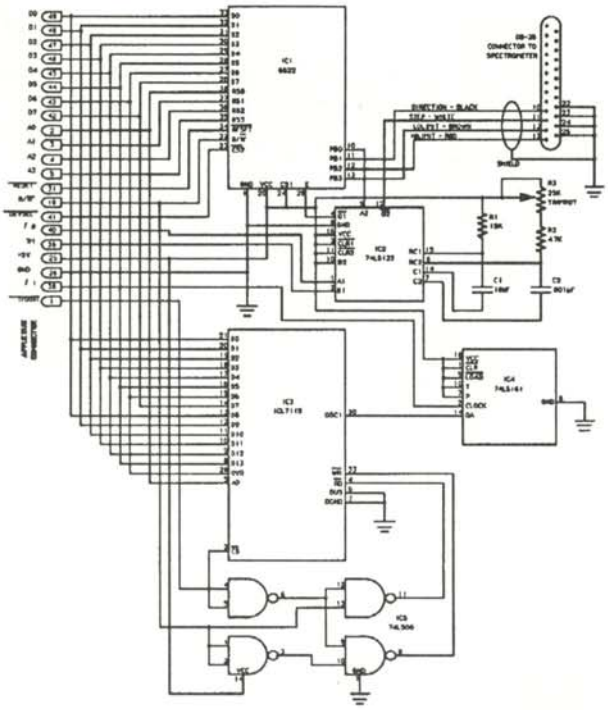

Figure 2
Digital circuits for the Apple IIe to mini-step driver interface.

pulse which steps the motor once; and a high- and low-wavelength limit switch signal which prevents grating rotation above or below predetermined wavelengths. The limit-switch outputs must be continually monitored while the grating is rotated. The direction bit level must remain constant during the grating rotation, and the pulse bit must switch from high to low for 2 - 10 microseconds to step the grating once. A signal amplifier of variable gain which places the photomultiplier signal in the 0 - 5 VDC range, an analog to digital converter and a stable DC power supply complete the system. All these pieces reside on a single interface board which occupies one slot on the Apple IIe.

Figure 2 shows the digital circuits of the interface. IC1 is a 6522 Versatile Interface Adapter (VIA) which generates and receives the spectrometer control signals. Only port A and the timer of the VIA are used. The VIA generates timing interrupts critical to the software used for data acquisition as well as the stepper-motor pulses. The data lines connect directly to the Apple data bus. The Apple address bus is connected to the VIA register select lines R_0 to R_3. The chip select signal on the VIA must remain stable for at least 140 ns before the rise of the clock. The clock and the device select pulse, unfortunately, are generated such that the reach the interface simultaneously. The solution to this problem is to delay the clock signal using IC2, a 74LS123 dual retriggerable one-shot.[7] IC2 also utilizes line PB0 of the VIA to generate the step-pulses for the mini-step driver.

IC3 is an analog to digital converter (ADC) that converts the amplified analog signal from the photomultiplier to a 14 bit digital number.[8] The Apple IIe data bus is 8 bits wide, so the ADC output must be accessed twice and then stored appropriately. The first read samples bits 0 to 7, while the second read samples bits 8 - 13 and the overrange bit OVR. Bit 7 is ignored on the second read. This ADC requires a 500 kHz clock that is generated by IC4, which divides the 1 MHz clock produced by the Apple IIe by a factor of 2. IC5 splits the R/W signal on the Aplle IIe bus into separate RD and WR signals required by the ADC. This chip also is used to decode the I/OSEL signal so that the ADC responds only to certain bus addresses.

Figure 3 shows the analog circuits for the spectrometer interface. This circuitry filters the signal output of the amplifier, amplifies the signal by a factor of 5, and provides a buffer between the two amplifiers. Diode D1 provides overload protection while resistor R4 and capacitor C3 filter out noise higher in frequency than the ADC conversion rate. Resistor R10 provides a zero offset for the input signal. The ADC requires a stable reference voltage which is produced by diode D3, a very stable temperature corrected voltage reference. When D3 is connected to -8VDC through R12, a voltage of about -6.9 VDC is produced. R13 divides this voltage to -5.00VDC. This reference voltage is then buffered by IC8a and fed into the ADC.

To function properly, the analog circuits and the ADC must be supplied with stable, clean power sources. Figure 4 shows circuits designed for this purpose. The input is ±12 VDC from the Apple IIe expansion slot, while the output is ±8VDC or ±5VDC. The circuit uses LC filters and ICs 9-12 selected from the LM78XX and LM79XX family of voltage regulators. Only the ADC and analog circuit components are powered from the on-board power supply. These components need to be insulated from digital switching noise present on the power lines available from the Apple IIe bus. IC3 requires both

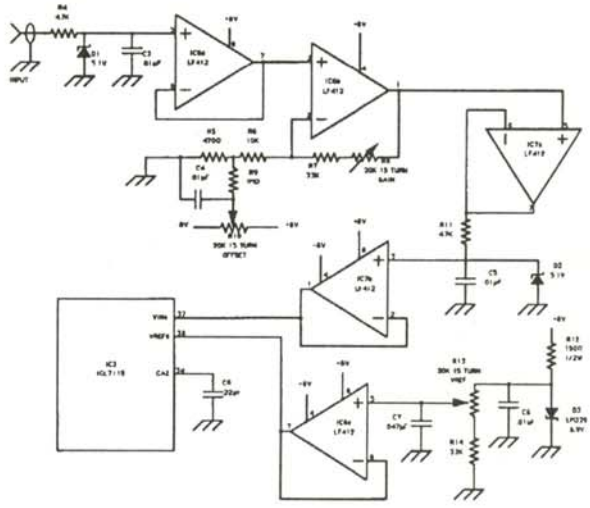

Figure 3
Analog cricuits for signal buffering, amplification and filtering. This circuit also produces a stable voltage reference for the ADC.

a digital and analog ground. Figure 4 also shows the decoupling capacitors that are placed as close as possible to the indicated IC.

All circuits in Figures 2-4 were constructed on a prototyping card using wire and solder connections and IC sockets. The digital circuits were placed as close as possible to the card edge connector, while the analog section utilized leads as short as possible. The card is calibrated by adjusting R_{13} to produce 5.00 Volts at pin 38 of IC3 and adjusting the offset voltage using R_{10} so that the output of the ADC is 0 when the input is grounded. Finally, the analog amplifier gain is adjusted using R8 so that a 1.000VDC analog input produces a binary output from the ADC centered at 16383, the maximum count without the OVR bit.

We used two other hardware enhancements to the Apple IIe. To speed numerical computations for spectral smoothing and deconvolution and to produce rapid updating of the video display, we used a 3.6MHz accelerator card [9]. Our software required memory expansion to 1 megabyte which we did with a commercially available card [10]. Our data station uses the usual Apple monochrome monitor, a disk drive, a printer with buffered interface and a graphics plotter. [11] Since all but two of the Apple's expansion slots are used, it is necessary to use a cooling fan.

SOFTWARE DESCRIPTION

The controlling software for our data system is a compiled BASIC host program which directs control to several other compiled BASIC programs.[12] The various BASIC programs, in turn, may call one or more assembly language subroutines. These subroutines, designed for execution speed, are used for initializing memory banks, displaying graphics and text on the double high resolution video screen, stepping the spectrometer grating, exchanging data between main and auxiliary memory, acquiring data and performing arithmetic operations

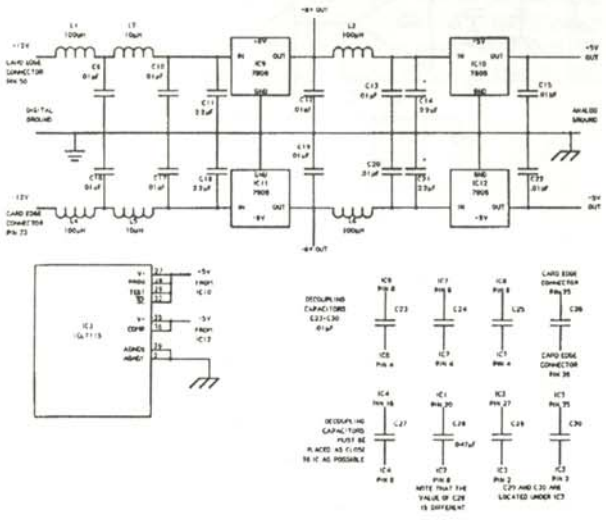

Figure 4
Voltage regulator circuits.

required for deconvolution and smoothing.

The 1 megabyte memory expansion is organized into 16 banks of 64K. Nine of these banks are reserved for spectra containing data taken at up to a maximum of 24,200 wavelength steps. Each spectral data point requires both a high and a low byte. The remainder of the memory bank is reserved for commentary information and parameters which record the conditions of data acquisition and any subsequent operations (e.g., smoothing) on the data. Of the remaining 7 auxiliary memory banks, 5 are used as RAM disks to facilitate rapid access to programs and subroutines; the remaining 2 banks are reserved for use by convolution assembly-language routines and for double high resolution (DHR) video memory.

Our software supports the DHR mode available on most Apple IIe units. This mode doubles the number of available columns so that one can display a matrix of 560 x 192 pixels. We found this mode valuable for displaying spectral detail. We utilized many programming techniques for the DHR display already published. [13]

DATA STATION OPERATION

The central piece of the software is the main menu, which gives the operator a choice of 9 different options.

1) Calibrate Spectrometer Position-
Allows the user to calibrate the spectrophotometer using the calibration dial or a standard emission line.

2) Manual move-
A key press will scan the spectrometer towards increasing or decreasing wavelengths at 10 speeds between 0.01 to 10 Å in the first order. Instantaneous wavelength and detector output are displayed. The software maintains the calibration by counting the accumulated number of steps forward or backward from the calibration point. If the desired wavelength is lower than the current wavelength, the software slews 200Å lower than the required value, stops, reverses, and then reaches the desired final position from the lower wavelength to eliminate mechanical backlash.

3) Acquire Data Automatically-
The operator inputs a list of parameters (scan rate, sampling step size, wavelength interval, etc.) which define the data to be measured. A memory bank to receive the spectrum is designated. Once the operator is satisfied with the input parameters, the grating is slewed to the starting position once again approaching from lower wavelengths to eliminate mechanical backlash. The grating is advanced one step and the detector signal is digitized and placed into memory. At the fastest scan speed available, two separate conversions are actually averaged before storage. As the scan speed is slowed, the number of averaged conversions increases to 256. The assembly language subroutine also samples the status of the high and low limit switches and decides if the scan should continue.

4) View Data in Memory-
This feature displays the full spectrum or partial spectrum in a bank. Any combination of 1% of the ordinate and 40 grating steps may be expanded to full scale. The operator may select a movable wavelength marker, which, when placed on any column of pixels, causes the corresponding wavelength and intensity to be displayed The operator can overlay up to three other spectra over

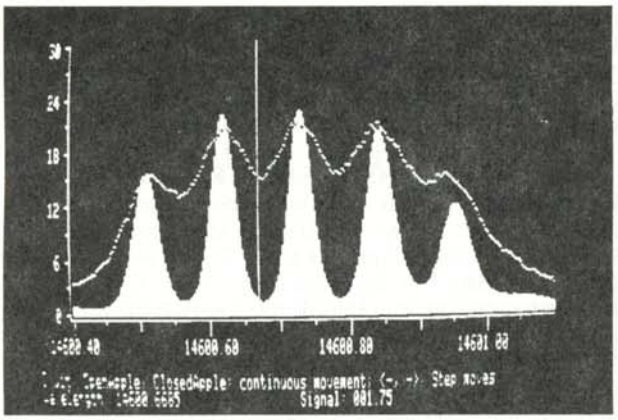

Figure 5
An example of the video output of View Data, showing the marker and overlay options.

the primary one, provided that all wavelength ranges and sampling densities are identical. Figure 5 is a photograph of the monitor displaying an example output of View Data. The spectrum shows the Zeeman splitting of the 6^3D_3-6^3P_2 emission line of Hg at about 3650Å obtained in the forth order of a 1200 lines/mm grating. The primary display has been smoothed and deconvolved, while the overlay is the raw data. Note the marker and the spectral detail provided by the DHR mode. A plotter option is available that produces 8.5" x 11" or 11" x 17" plots or transparencies of the primary spectrum and one overlay in up to three colors. Figure 6 shows an example of the plotter output of the six components of the Zeeman splitting of the 7^3S_1-6^3P_1 emission line of Hg taken in the third order. The graph shows the data both as observed directly and after digital smoothing and deconvolution. The software for this section utilizes a BASIC host. The operator selects and edits parameters required for the video display or plot. These parameters are poked into memory locations expected by the graphics assembly-language subroutines which are in turn called by the host. We developed our own graphics primitives to plot points, draw lines and display characters. As Figure 5 demonstrates, the DHR can display a pleasing amount of spectral detail. With compiled BASIC and the accelerator card, the screen update requires less than 1 second.; without the card and in interpreted BASIC, the speed was unacceptably slow. A plot requires approximately 2 minutes.

5. The Filer-

This selection allows the operator to load data from a floppy disk to the Aux memory bank, to save data from a bank to a disk, to catalog a disk, to delete data from the disk and to transfer a spectrum between one Aux memory bank and another. Error traps are provided to prevent the operator from performing unwanted deletions, overwriting data or saving different spectra with the same file name. The operator interacts with a compiled BASIC host which pokes the necessary parameters into memory locations and then calls assembly-language subroutines which accomplish the required operations.

6. Edit Commentary Information-

This selection allows the operator to change the name of a data set and the commentary information. Such parameters as the number of steps per Ångstrom or scan speed cannot be changed by the operator as they are a characteristic of the data.

7. Baseline Adjust-

This routine permits the operator to subtract a fixed intensity unit from the intensity values recorded at each wavelength of a data set and then to multiply every intensity value by a scaling parameter. Baseline adjust retains the original data bank and creates a new one with the modified data.

8. Quartic Smooth-

To reduce the noise present in a spectrum, we repeat conversions and average the signal at fixed wavelengths before storage in a data array. In addition, we incorporate an operator-selectable option of digital smoothing. We calculate the quartic smoothing function [14] containing 2N+1 components, where 2N+1 is the number of wavelength steps in the full width at half height (FWHH) of an isolated line in our spectrum. We next convolve this smoothing function with itself, and in turn, convolve the resulting function with itself. This final smoothing function is used in a convolution operation accomplished by an assembly-language subroutine to smooth a data set. This approach is equivalent to four successive quartic smoothing operations and is significantly faster. The smoothing of a 2000 point spectrum with a 40 point quartic smoothing function requires about 30 seconds. Figure 6 shows an example of this smoothing process.

9. Deconvolution -

Our data system can enhance the resolution of a spectrum using a deconvolution process. [15] We use a Gaussian instrumental response function with of half-width described above and a weighting function. [16] The operator selects the data set to be deconvolved, the empty bank of Aux memory to be used to receive the deconvolved spectrum, the number of grating steps in the FWHH of the response function, and the number of iterations. The operator can elect to follow the convergence by printing out the r.m.s. error between the observed data and the convolution of the kth iteration of the deconvolution process with the response function. Typical deconvolutions re-

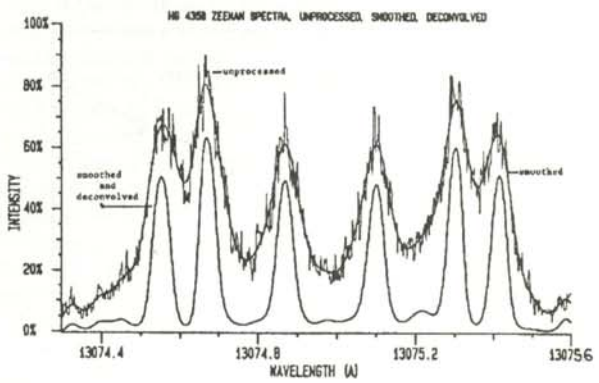

Figure 6
An example of the plotter output. The Zeeman splitting of the 4358Å Hg line, observed in the third order. Also illustrated are the results of the smoothing and deconvolution operations.

quire no more than 40-50 iterations. Figure 6 is an example where the primary spectrum has experienced two baseline operations, smoothing and deconvolution. One deconvolution iteration of a 2000 point spectrum with a 40 point response function requires about 30 seconds. The baseline, smooth and deconvolution operations automatically produce or update an unalterable process string appended to each data file.

TEST OF THE SYSTEM

The Zeeman splitting of the 4358Å Hg emission line provides a test of the performance of the smoothing and deconvolution features. A polaroid filter oriented parallel to the applied magnetic field will transmit the central ($\Delta M_J = 0$) two components of the pattern and suppress the others. The wavelength separation $\Delta\lambda$ of the two components should vary linearly with the current in the magnet. We can use this fact to test our system. Figure 7 shows a plot of $\Delta\lambda$ vs the current in the magnet. The spectra were measured in the third order and their wavelength separations divided by 3 to obtain $\Delta\lambda$. Figure 7 shows that although a non-zero $\Delta\lambda$ appears in the raw data down to 0.6 amps, its measured value is too small (as expected) and that appreciable errors in raw data values begin at ≈0.04Å By contrast, the graph indicated that values obtained after smoothing and deconvolution are reliable for separations as small as 0.0225Å. The non-zero y-intercept of Figure 7 is caused by a permanent residual magnetization of the iron-core magnet.

SUMMARY

This paper describes a computer-based data station for emission spectrophotometers. We presented a series of circuit diagrams and generally describe software which permits an enhanced Apple IIe microcomputer to control the spectrophotometer and record and process its output. Data storage, retrieval, scaling, baseline adjustment, digital smoothing, deconvolution, video display and plotter output are available.

The novel features of this work include relatively fast performance from a limited microprocessor and low cost. The hardware components for the custom interface card cost under $100, while the total hardware cost for the entire system is about $3,000. The most expensive component, the plotter, costs about 40% of the total. The system performance compares favorably with much more expensive commercially-available computer data stations.

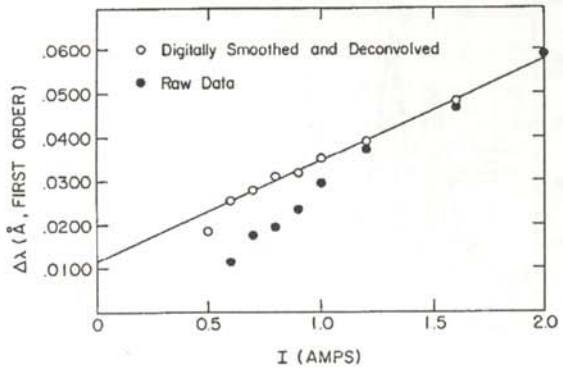

Figure 7

Test of the smoothing and deconvolution operations using the $\Delta M_J = 0$ components of the Zeeman splitting of the 4358Å line of Hg. $\Delta\lambda$ is the wavelength separation of the components and I is the electromagnet current.

ACKNOWLEDGMENTS

Partial support for this work was provided by the National Science Foundations's College Science Instrumentation Program through grant #8551175 and by the Centre College Faculty Development Committee. Centre College undergraduate Ray Pribble recorded the measurements displayed in Figure 7. The author wishes to thank Professor Frank DeLucia, formerly of the Physics Department of Duke University, for the gift of the electromagnet used to produce the Zeeman spectra. He also wishes to thank Dr. Marshall Wilt for providing encouragement and direction for this project.

REFERENCES

* Present address of author: MIT Laboratory for Computer Science, 545 Technology Square, Cambridge, MA 02139, mikec@lcs.mit.edu

1. J.E. Wampler, Appl. Spectrosc. Rev., 17, 1981, p. 407.
2. E. Ziegler, Anal. Chim. Acta, 147, 193, p. 77.
3. H.E. Korth, J. Phys., Colloq., C10, 1983, p. 10
4. P.B. Farnsworth and J.P. Walters, Anal. Chem. 54, 1982, p. 885.
5. P. Trousson, Rev. Sci. Instrum., 55, 1984, p. 1989.
6. An Apple IIe microcomputer interfaced to a SPEX model 1704 spectrometer (Spex Industries, Metuhen, NJ) with a photomultiplier detector and a Pacific Instruments Model 124 signal amplifier (Pacific Instruments, Conrad, CA).
7. L. Korba, Byte, 7, 1982, p. 520.
8. ICL7115 Analog to Digital Converter (Intersil, Cupertino, CA.
9. Accelerator IIe, a 3.6 MHz accelerator card from Titon Technologies, Ann Arbor, MI.
10. Ramworks II card from Applied Engineering, Carrollton, TX.
11. Hewlett-Packard HP 7475A Graphics Plotter (San Diego, CA) interfaced through a serial interface card (Messenger, by Perisoft, Santa Clara, CA).
12. TASC complier by Microsoft, Bellevue, WA.
13. P. Baum and L. Roddenbery, Softalk, September 1983, p. 83.
14. P.D. Willson and T.H. Edwards, Appl. Spectrosc. Rev. 12, 1976, p. 1.
15. W.E. Blass and G.W. Halsey, "Instrumental Considerations", in Deconvolution with Applications to Spectroscopy, P.A. Jansson, Ed. Academic Press, New York, 1984, Chapter 6, pp. 153-185, especially Equation 52.
16 W.E. Blass and G.W. Halsey, "Deconvolution Examples", in Deconvolution with Applications to Spectroscopy, P.A. Jansson, Ed., Academic Press, New Yorik, 1984, chapter 7, p. 204, Equations 5 and 6.

FACULTY SPONSOR

Professor Marshall Wilt
Physics Department
Centre College
Danville, KY 40422

STUDY OF THERMALLY STIMULATED CURRENT IN UNDOPED AND FE-DOPED BISMUTH GERMANIUM OXIDE

Keith L. Chappell *
Department of Physics
University of Central Oklahoma
Edmond, OK 73034
received May 20, 1992

ABSTRACT

Exposing undoped $Bi_{12}GeO_{20}$ (BGO) at liquid nitrogen temperatures to broad-band light from an Xe lamp or narrow-band light at 1.96 eV or 2.28 eV from a laser produces thermally stimulated currents (TSC). Major current peaks at 175 K and 285 K were observed following exposure to the Xe light. These peaks are in good agreement with previous results. The high temperature current peaks that result from the electrons thermally escaping from the traps and returning to the donors correlated with the anneal stage of the photochromic bands. The high temperature peaks were reduced when the lasers were used. When a Fe-doped BGO sample was illuminated with the Xe lamp, the major current peak was at 195K. This result matches the major anneal stage of the photochromic bands in Fe-doped BGO. No TSC signals were observed following exposure to the laser sources.

INTRODUCTION

The compound bismuth germanium oxide, $Bi_{12}GeO_{20}$ (BGO) is a photorefractive material that is widely studied for its potential for electro-optic applications. [1] Photorefractive materials are nonlinear in nature such that light changes the index of refraction of the material. The light affects how fast the light travels through it. They act much like film emulsions. They change rapidly when excited with intense light, but unlike film, the "patterns" are erasable. Images can be created or removed by design.

The properties of BGO are similar to those of the closely related compound bismuth silicon oxide, $Bi_{12}SiO_{20}$.[2,3] The photorefractive response present in BGO is due to charge transfer from light regions to dark and the capture of electrons by empty shallower traps. The charge distribution sets up an electric field which modifies the index of refraction through the electro-optic effect.[4] This information suggests the need to investigate trapping and migration utilizing thermally stimulated currents (TSC).[5,6]

Exposing BGO to light whose energy is near the edge of the band at low temperatures produces optical absorption bands extending from about 1.5eV to the band edge. [3] In the process, electrons are excited from deep donors to the conduction band, where they migrate until being trapped in shallower levels. The newly filled traps introduce an additional optical absorption which extends from the infrared to the absorption cutoff in the near ultraviolet. This photo-induced or photochromic absorption band arises from the optical excitation of the electrons back to the conduction bands.[3] Photochromic absorption bands are created in a nonlinear material when the light changes the amount of light that the medium can absorb. The bands are created at specific wavelengths of light at which the medium absorbs, giving rise to a different set of absorption lines. This is commonly seen in sunglasses that darken in bright sunlight and lighten in dark rooms. These results suggest that a study using TSC will add additional information about the thermal stability of the traps involved in the photochromic bands and the photorefractive effect.

EXPERIMENTAL PROCEDURE

The undoped and Fe-doped BGO crystals were grown at Oklahoma State University for this study. The starting materials were Johnson-Mathey Grade Bi_2O_2 and GeO_2. The materials were mixed in a stoichiometric ratio and then heated treated at 800 C for 48 hours in an oxygen atmosphere. The Fe-doping was accomplished by adding Fe_2O_3 with the related reduction of GeO_2. Single crys-

---

Keith Chappell graduated from the University of Central Oklahoma in May, 1992 with a Bachelor of Science in Engineering Physics. He is currently pursuing a Masters' degree in Electrical Engineering at the University of Oklahoma. He is doing research in the area of polymer-based electroluminescent devices. This project came out of research he did in the summer of 1991 at Oklahoma State University while participating in the National Science Foundation's Research Experience for Undergraduates (REU) program.

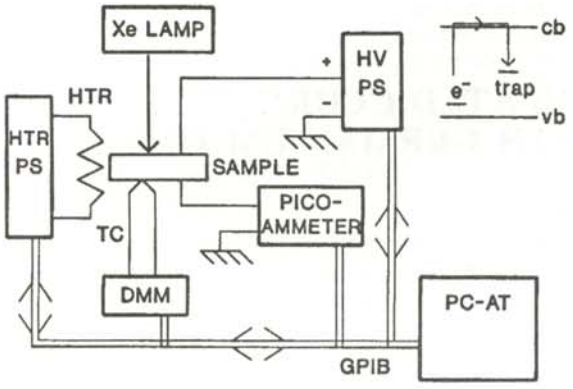

Figure 1
The layout, hookups and equipment used in this TSC experiment.

tals of BGO were grown in air using the Czochralski method on [100] seeds. The pull rate was 2.5 -3.0 mm/hr and the rotation rate was 30-86 rpm. The crystals showed the yellow coloration typical of BGO due to an absorption band or shoulder extending from about 2.5 eV to the absorption edge near 3.4 eV. [3] Optical samples were prepared from 1.1 - 1.2 mm thick slices of either [100] or [110] surfaces. Thin semitransparent electrical contacts were obtained using evaporated Au film. The effect of different geometries and materials have been shown to be minor. [7] Two thin brass contact strips were used to clamp the sample between sapphire wafers (for electrical isolation) in the optical cryostat. One strip had a small hole for the light source to excite the crystal. The sample was then mounted on the cold finger of an optical cryostat which could be cooled to liquid nitrogen temperature.

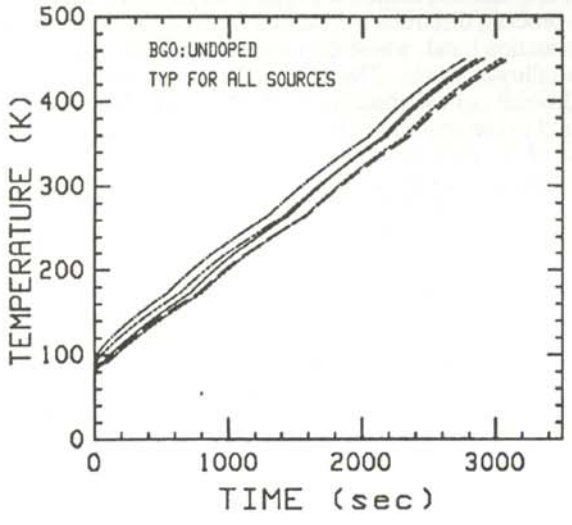

Figure 2
The five lines represent the heating rates of the undoped BGO sample with each different optical excitation for 1 hour each: no optical excitation; Oriel Xe source; 1.51 eV, 1.96 eV and 2.28 eV monochromatic laser light.

Figure 1 shows a block diagram of the experimental system. An electric field of 500 V/cm was established by the high voltage power supply. A picoammeter was used to collect the thermally stimulated current signal. The voltmeter was used to read the sample temperature using the thermocouple attached to the cold finger. A power supply programmer let us control the heater power supply. The instruments were connected to a personal computer by the General Purpose Interface Bus. The data were collected, stored and later plotted using the PC.

After the sample was cooled to liquid nitrogen temperatures, it was exposed for 1 hour to one of several light sources prior to the data collection run. The sources were an unfiltered Xe lamp, a 1.51 eV infra-red diode laser, and a 1.96 eV He-Ne laser, and a 2.28 eV green He-Ne laser. After exposure the sample was warmed to near 450 K at a nearly linear heating rate as shown in Figure 2. During the heating , the sample temperature and current were recorded as a function of time by the PC. This process was repeated for each illumination source. The entire process was repeated for the Fe-doped sample. A background signal, always less than .01 nA for temperature below 350K was measured prior to exposure to the light sources.

RESULTS AND DISCUSSION

Figure 3 shows the TSC results for the different optical excitation of the undoped BGO samples. The solid curve depicts the peaks produced by the Xe lamp at 170-180 K, 240 K and 290 K. The curve comprised of long dashes portrays the excitation which occurred at low temperatures using the 2.28 eV source. Absorption for this source was weaker at higher temperatures. The curve comprised of short dashes indicates that excitation was suppressed further at higher temperatures using the 1.96 eV source. No TSC peaks were observed when the sample was exposed to 1.51 eV light from the diode laser.

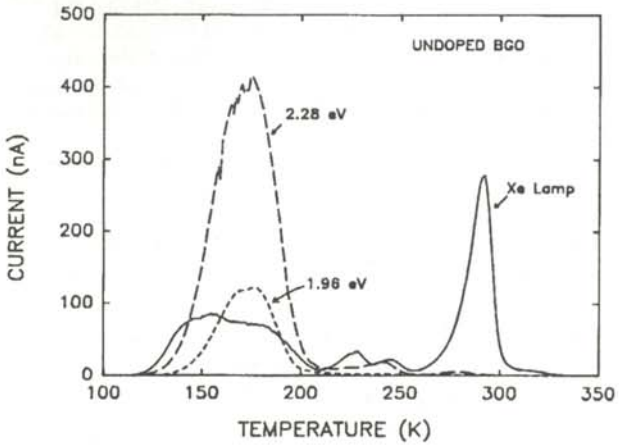

Figure 3
Plot of current vs temperature for the undoped BGO sample showing the TSC peaks.

Comparison of peak positions with previous work indicate good agreement. [2] Plotting the log of the current vs temperature enhances the peaks, as shown in Figure 4. The current peaks at 280K and above are much weaker when the TSC is produced by exposure to the 2.28 eV and 1.96eV lasers. Other results failed to observe photochromic bands following exposure to light with photon energy less than 2.4 eV. [3] This results suggests that these high temperature peaks are related to the decay of the photochromic bands.

An anneal study of the photochromic bands was carried out on the same samples that were used for the TSC experiments. The samples were mounted on the cold-finger of a closed cycle helium refrigerator. After they were cooled to about 10K, an optical absorption curve was taken. After the sample was exposed to 3 eV light, the absorption curve was re-measured. The sample was then heated to the desired anneal temperature, cooled back to 10K and measured again. This anneal process was repeated for temperatures up to about 300K. The contour plot in Figure 5 shows the results obtained for the undoped BGO sample. The major anneal stage near 250K agrees well with our TSC results on this sample.

Figure 6 shows the TSC curve using the Xe lamp on the Fe-doped sample. In contrast to Figure 4, the high temperature peaks are missing or suppressed. The overall signal is smaller as are the photochromic bands. TSC is not generated when either the 1.96eV or 2.28 eV laser is used. The doping with Fe appears to remove some of the absorption, but does not introduce additional photochromic bands. This suggests that Fe may act as a trap and is in good agreement with previous work. [3]

The contour plot in Figure 7 shows the anneal of the photochromic bands in the same Fe-doped BGO sample used for our TSC study. A major decrease is seen from 100 - 200 K. This parallels the major current peaks seen in Figure 6.

In a more detailed analysis of TSC data, the use of monochromatic laser light appears to have an advantage due to the increase in intensity. Further work is required in order to determine trap depths by taking several TSC runs with different linear heating rates to construct a Hoogenstraaten plot. [8]

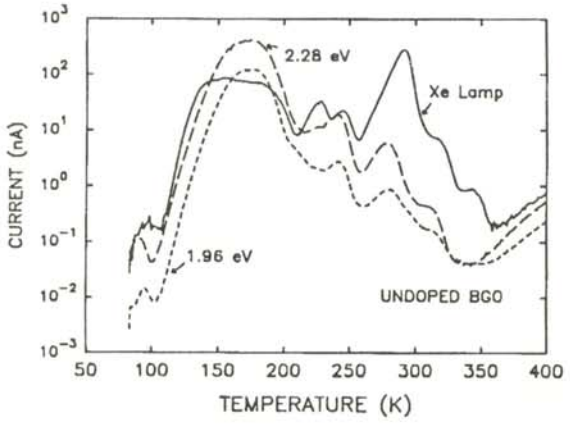

Figure 4
Log of current vs. temperature for undoped BGO. This shows the TSC peaks for the laser light.

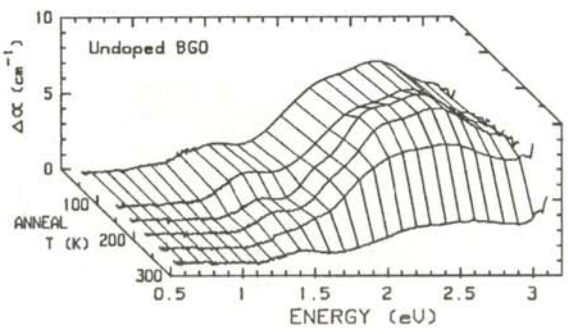

Figure 5
Thermal decay of the photochromic bands in undoped BGO.

ACKNOWLEDGMENTS

This work was supported by the National Science Foundation REU program and Rome Laboratories, USAF, Hanscom AFB, MA 01731. Special thanks go to JJ. Martin for his advice in the experimental setups and patience and to B. Jassemnejad for helpful discussions.

REFERENCES

* Current address of author: School of Electrical Engineering, University of Oklahoma, 202 W. Boyd, Room 218, Norman, OK 73019-0631, klc@essex.ecn.uoknor.edu.

1. B.A. Horwitz and F.J. Corbett, Opt. Eng. 17, 1978, p. 353.

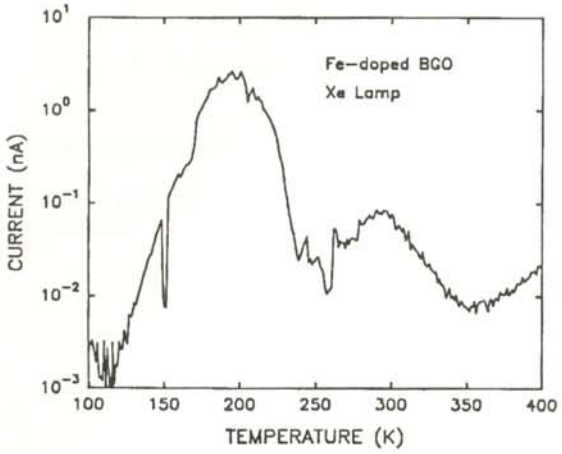

Figure 6
Log of current vs temperature for Fe-doped BGO. Comparison with Figure 4 shows the effect of the doping.

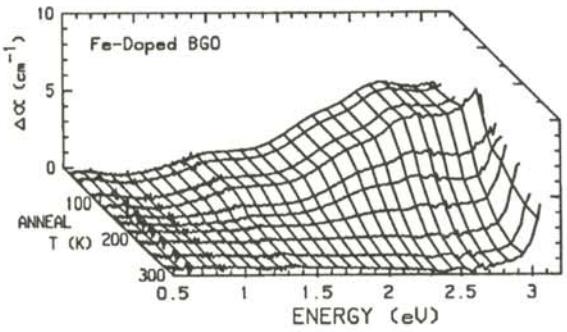

Figure 7
Thermal decay of the photochromic bands in Fe-doped BGO.

2. T. Takamori and D. Just, J. Appl. Phys., 69, 1991, p. 3958.

3. J.J. Martin, I. Foldvari and C.A. Hunt, J. Appl. Phys., 70, 1991, p. 7554.

4. D.M. Pepper, J. Feinberg and N.V. Kukhtarev, Scien. Amer., Oct, 1990, p. 62.

5. R.B. Lauer, J. Appl. Phys., 42, 1971, p. 2147.

6. S. M. Efendiev, V.E. Bagiev, A.K. Zeinally, M. Garandolfo and P. Vecchia, Ferroelectronics, 43, 1982, p. 217.

7. T. Takamori and D. Just, J. Appl. Phys., 67, 1990, p. 848.
8. W. Hoogenstraaten, Philips Res. Rep., 13, 1958, p. 515.

FACULTY SPONSOR

Dr. Joel J. Martin
Department of Physics
Oklahoma State University
Stillwater, OK 74078-0444

DYNAMICS OF A SYSTEM OF TWO COUPLED NON-LINEAR OSCILLATORS

Jeffrey L. Rogers
Department of Physics
Florida Atlantic University
Boca Raton, FL 33431
received 3/21/92

ABSTRACT

This article is an examination of two coupled non-linear limit-cycle oscillators. Numerical simulations are used in conjunction with analytical calculations to identify three distinct forms of behavior: mode locking, amplitude death and quasi-periodicity. The boundaries in parameter space are found and the equations of motion for all three types are presented.

INTRODUCTION

The use of oscillators to model phenomena may be found throughout physics. Light, phonons and plasmons are just of few of a great wealth of examples. The use of linear differential equations to define the elements in the oscillator model mean that the powerful tools of integrable differential equations can be used to understand the phenomena.

Oscillators that use non-linear differential equations have been used as a modeling technique. While these equations lose many of the tools of integrable differential equations, they are capable of describing a wider range of system behaviors. Some diverse applications in biology include synchronous firing of large groups of fireflies, chirping patterns among groups of crickets, cardiac rhythms or synchronization of menstrual cycles in groups of women.

The drawback to using non-linear models is often the loss of concepts such as superposition of solutions. Each non-linear model possesses unique abilities as well as unique obstacles to finding its solution. Several authors have examined non-linear models of various types and with different representations of coupling. [1-3,5-7,9] They have made substantial progress in understanding and applying such models. This research is part of an ongoing project into the three and N oscillator problems as well as the use of parallel and vector computers for performing simulations.

MODEL

We are concerned with a system of two limit-cycle oscillators, each given by the equation[3]:

$$\frac{dZ}{dt} = Z\,(1 - |Z|^2 + i\omega)\,, \tag{1}$$

which is derived from the van der Pol equation [4]. Z is a complex number and ω is a frequency. A representation of two coupled limit-cycle oscillators may be:

$$\begin{aligned}\frac{dZ_1}{dt} &= Z_1\,(1 - |Z_1|^2 + i\omega_1) + \frac{k}{2}\,(Z_2 - Z_1)\,,\\ \frac{dZ_2}{dt} &= Z_2\,(1 - |Z_2|^2 + i\omega_2) + \frac{k}{2}\,(Z_1 - Z_2)\,.\end{aligned} \tag{2}$$

where k is a coupling constant.

To assist in solving these equations, we introduce an order parameter [1-3,5]:

$$Re^{i\phi} = \frac{1}{2}\sum_{j=1}^{2} Z_j \tag{3}$$

that is a sum of the elements. The order parameter is sensitive to changes in both amplitude and phase. The magnitude R is an indication of the degree of order present in the system. R is defined such that |R|=1 corresponds to elements of amplitude 1 and equal phase while |R|= 0 corresponds to elements of amplitude 0 or of equal magnitudes and phase difference π.

Jeff graduated with a Bachelor of Science degree in Physics at the conclusion of the spring term of 1992. He is currently working towards a graduate degree in Mathematical and Computational Physics at Florida Atlantic University. He is continuing his research in non-linear dynamics and is pursuing his lifelong ambition of surfing Backdoor Pipe standing up on the first reef at 6 to 8

NUMERICAL RESULTS

To find out how the system develops in time, the coupled Equations 2 were integrated numerically. We used a fourth order Runge-Kutta algorithm[8]. The integration proved to be stable with a step size of 0.01. Most of our calculations were performed on a Decstation 3100 at Florida Atlantic University. We also did some calculations using the Cray YMP/432 at Florida State University. We varied initial conditions and used step sizes as small as 0.001. Depending upon the values of k and ω chosen, the system evolved into three types of behavior:

1) Mode locking

If $k \leq 2$ and $k \geq \omega$ or if $k > 2$ and $k > (1 + 1/4\omega^2)$, mode locking, shown in Figure 1, occurred. This is characterized by the oscillators rotating with the same frequency about a limit-cycle $|Z_j| > 0$. The oscillators maintained a constant phase difference and angular velocity. The order parameter quickly settled to a fixed value less than one determined by the phase angle difference and the amplitudes.

2) Amplitude death

When $k \leq (1 + 1/4\omega^2)$ and $k > 2$, amplitude death, shown in Figure 2, occurred. It is characterized by the system collapsing to the origin as time moves toward infinity. The oscillators pull one another down, causing the origin to be a stable solution for the equations. The order parameter, being dependent on both phase and position, tended to zero as time increased. Amplitude death has been examined by several authors.[2,3,7,10]

3) Quasi-periodicity

If $k < \omega$ and $k < 2$, quasi-periodic behavior, shown in Figure 3, occurs. It is characterized by a circle of constant radius precessing about a limit-cycle leading to a rosette-like patter where R oscillate between two values in a regular fashion. The magnitude of the oscillation is constant and dependent on the frequency ω. The amplitude and phase are time dependent.

ANALYSIS

Before attempting to analyze the system given by Equation 2, it is prudent to first understand the behavior of one uncoupled non-linear oscillator, Equation 1 can be solved by a separation of variables. The solution is:

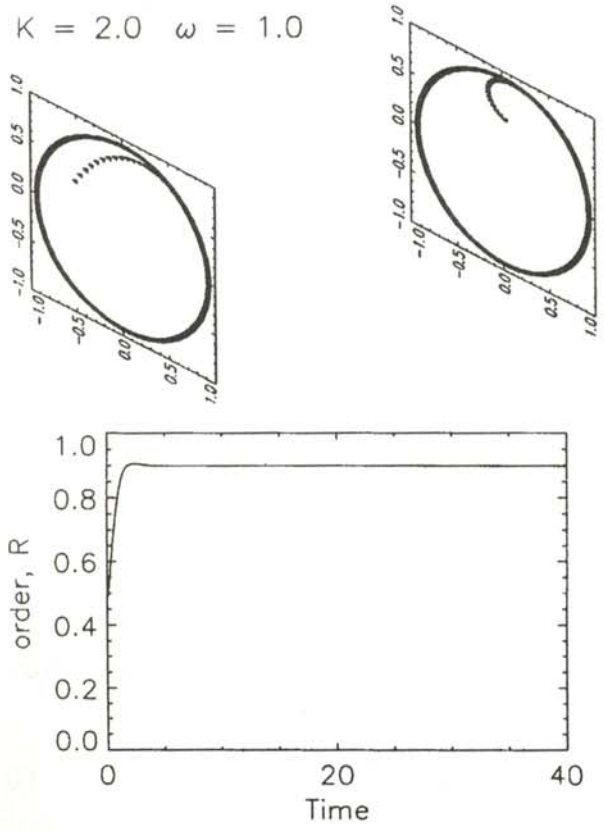

Figure 1

Top *- Real vs. imaginary components of Z_j, demonstrating mode locking. Each triangle represents the position of the jth oscillator at a particular time.*

Bottom *- The magnitude of the order parameter R as a fucntion of time. In the case of mode locking, R quickly locks onto the constant value.*

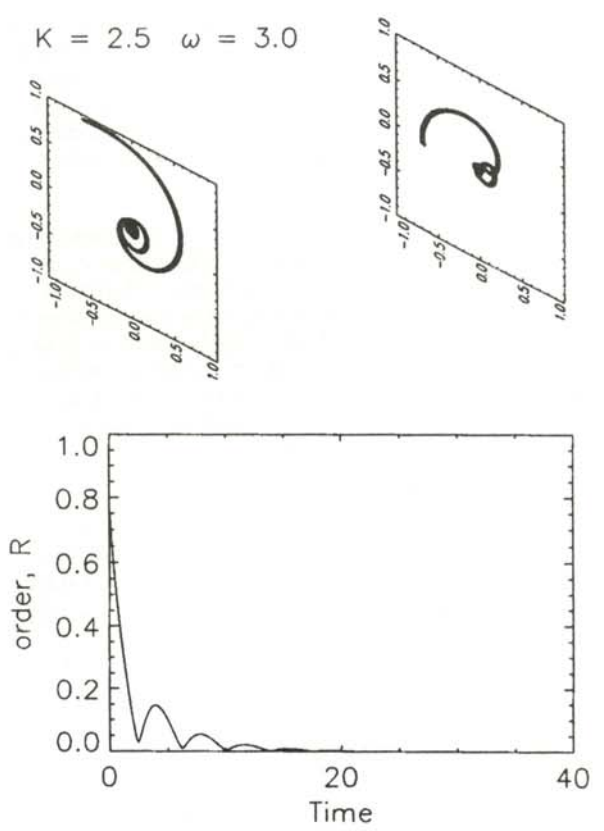

Figure 2

Top *- Real vs. imaginary components of Z_j, demonstrating amplitude death. The elements settle on the origin, which is a stable solution.*

Bottom *- The magnitude of the order parameter R as a function of time. As the oscillators settle on the origin, their amplitudes tend to zero, thus R tends to zero.*

$$Z = \sqrt{\frac{1}{2} e^{t+c} \operatorname{sech}(t+c)}\ e^{i\omega t} \qquad (4)$$

In the limit as time becomes large, |Z| -> 1, independent of initial conditions. Equation 4 then becomes the attracting solution, $Z = e^{i\omega t}$, the equation of a limit-cycle oscillator moving with frequency ω. The origin is always an unstable solution to Equation 1.

The coupling terms in the two oscillator case do not allow for such a straight forward analysis. We use what was learned from the numerical simulations and the analysis for one oscillator to make an assumption about the solutions of the case of two oscillators. In this manner we can find the conditions which must exist for the solutions to be valid. Moving into a rotating frame of reference with $\omega = \omega_1 - \omega_2$ and setting $|Z| = |Z_1| = |Z_2|$, Equation 2 becomes:

$$\frac{dZ_1}{dt} = Z_1 (1 - |Z|^2 + i\omega_1) + \frac{k}{2} (Z_2 - Z_1) , \qquad (5a)$$

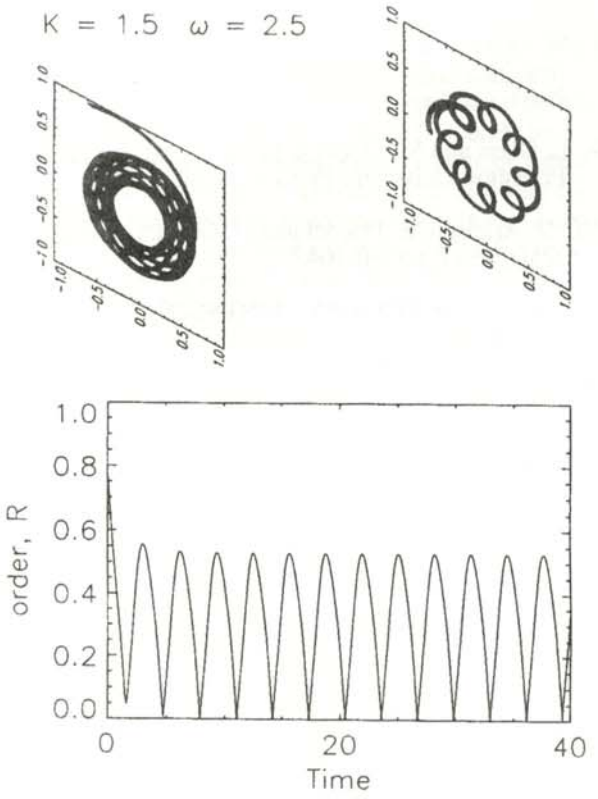

Figure 3

***Top** - Real vs. imaginary components of Zj, demonstrating quasi-periodicity. This is the most complicated of the three forms observed. Both the magnitudes and phase differences are time dependent.*

***Bottom** - The magnitude of the order parameter R as a function of time. R oscillates between two fixed values.*

$$\frac{dZ_2}{dt} = Z_2 (1 - |Z|^2) + \frac{k}{2} (Z_1 - Z_2) . \qquad (5b)$$

Assuming solutions $Z_1 = \rho e^{i\alpha}$ and $Z_2 = \rho e^{i\beta}$ leads to the following set of equations:

$$\frac{1}{\rho}\frac{d\rho}{dt} = 1 - \rho^2 - \frac{k}{2} + \frac{k}{2}\cos(\beta - \alpha) , \qquad (6a)$$

$$-\frac{d\{\beta - \alpha\}}{dt} = \omega + k \sin\{\beta - \alpha\} , \qquad (6b)$$

$$\beta + \alpha = \omega t , \qquad (6c)$$

where $\rho = |Z|$ and α and β are phase angles. In the general case, all three are considered to be time dependent. The boundaries between the three types of behavior in k-ω space are found by analysis of these conditions.

MODE LOCKED

Oscillators that are mode locked were observed numerically to have time-independent magnitude ρ and phase difference β−α. Equation 6a gives the magnitude:

$$\rho = \sqrt{\frac{1}{2}\left(2 - k + \sqrt{k^2 - \omega^2}\right)} . \qquad (7)$$

Equation 6b predicts that the boundaries to be $k \le 2, k \ge \omega$ and $k > 2, k > (1 + 1/4\omega^2)$. The conditions given by Equation 6 will produce the solution for mode locking

$$Z_1 = \sqrt{\frac{1}{2}\left(2 - k + \sqrt{k^2 - \omega^2}\right)}\ \exp\left[\, i\frac{1}{2}\left(\omega t + \sin^{-1}\left\{-\frac{\omega}{k}\right\}\right)\right], \qquad (8)$$

$$Z_2 = Z_1\, e^{i\Theta} ,$$

where Θ is some constant corresponding to the difference in phase.

AMPLITUDE DEATH

Amplitude death may be thought of as a special case of mode locking, so the same condition equations may be applied. These equations give the boundaries as $k > 2$, $k \ge (1 + 1/4\omega^2)$. This is the one solution which is trivial. The time derivative of the position is zero, so the system evolves to the fixed point solution $Z_1 = Z_2 = 0$. In this region, the origin is a stable solution for the system. This stability, in contrast to the one oscillator case where the origin is an unstable solution, can be attributed to the coupling.

QUASI-PERIODICITY

Periodicity exists in the region of k-ω space where the simplifying assumption that the magnitude ρ and the phase difference β−α are independent of time cannot be made. However, the previous analysis still may be used to determine the boundaries: $k < 2, k < \omega$. Integrating Equation 6b in its general form and substitution of Equa-

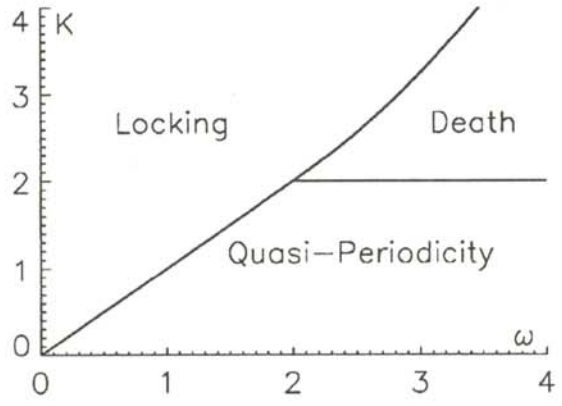

Figure 4
Regions of k-ω space where the three forms of behavior of Equation 2 reside.

tion 6c where necessary, leads to the solutions for the phase angles α and β:

$$\alpha = \frac{1}{2}\omega t - \eta$$

$$\beta = \frac{1}{2}\omega t + \eta \qquad (9)$$

$$\eta = \tan^{-1}\left[\frac{1}{\omega}\left(\sqrt{\omega^2 - k^2}\,\tan\left\{\frac{\sqrt{\omega^2-k^2}}{2}\right\}t - k\right)\right]$$

The remaining unknown quantity is the magnitude of ρ for periodicity. This can be found by solving the differential equation resulting from substituting Equations 9 into Equation 6a.

Figure 4 shows the areas of k-ω space where the three forms of behavior reside. The numerical and analytical results are in exact agreement as to the boundaries.

SUMMARY

The combination of numerical simulation and analysis is a fruitful tool for predicting the behavior of non-linear oscillators in k-ω space. Despite the non-linearity of the equations, this combination of methods allows the equations of motion to be found. The sole use of either method would not have been so successful. The analytical approach would stall due to the non-integrability of the original equations, while the numerical simulations would become tedious, leaving questions as to whether the results are complete or even correct.

ACKNOWLEDGMENTS

The author would like to thank Drs. J.R. Cox, J.M. Freeman, A.J. Mandell, J.B. McGuire for their conversations, guidance and assistance. Dr. L.T. Wille was the author's advisor and gave him the opportunity to experience research. His assistance has been crucial and the author would like to thank him for the support. He also wishes to thank the Supercomputer Computation Research Institute at Florida State University for access to the Cray computer.

REFERENCES

1. A. Winfree, The Geometry of Biological Time, Springer, New York, 1980.
2. Y. Aizawa, Prog. Theo. Phys. 56, 1976, pp. 703-716.
3. P. Matthews and S. Strogatz, Phys. Rev. Lett., 65, 1990, pp. 1701-1704.
4. M. Lax, Brandeis University Summer Institute in Theoretical Physics, Gordon and Breach, New York, 1968.
5. Y. Kuramoto and I. Nishikawa, J. Stat. Phys. 49, 1987, pp. 569-605.
6. H. Daido, Phys. Rev. Lett., 61, 1988, pp. 231-234.
7. R. Mirollo and S. Strogatz, J. Stat. Phys., 60, 1990, pp. 245-263.
8. W. Press, B. Flannery, S Teukolsky and W. Vetterling, Numerical Recipes, Cambridge University Press, Cambridge, 1988.
9. L. Glass and M. Mackey, From Clocks to Chaos, Princeton University Press, Princeton, 1988.
10. D. Aronson, E. Doedel and H. Othmer, Physica, 25D, 1987, pp. 20-104.

FACULTY SPONSOR

Dr. L.T. Wille
Department of Physics
Florida Atlantic University
Boca Raton, FL 33431
(407)367-3379
willel@fauvax.bitnet

LASER OPTOGALVANIC SPECTROSCOPY OF NEON

Douglas B. Brann
Department of Physics
University of Northern Colorado
Greeley, CO 80639
received May 10, 1992

ABSTRACT

The highly excited electronic states of a neon atoms are examined using laser optogalvanic spectroscopy. The experiment uses a flashlamp pumped tunable dye laser and a hollow cathode discharge cell to examine the electronic absorption lines. A computer was used to simultaneously record the power of the laser, a reference iodine absorption spectrum and the optogalvanic spectrum being studied. The hardware and software used to run the experiment are discussed as are the results of the experiment.

BACKGROUND

The purpose of this research project was to design, build and use an experimental apparatus to examine the molecular bands of compounds containing transition metals. We intended to investigate the effect of d-orbitals on the bonds of titanium oxide and aluminum(I) fluoride by sputtering the molecules within a hollow cathode tube while shining laser light on the tube. The resulting optogalvanic signal would be observed and stored on a computer. Much of the hardware and software needed for this experiment already existed, but extensive modification and assembly were required to produce a sensitive, yet inexpensive experimental apparatus which would be capable of detecting and displaying electronic changes in molecular spectra for neon, sodium, potassium, calcium and copper.

The inert gas in many of the optogalvanic cells is neon. Initially, we decided to examine the spectrum of neon since it is monatomic and already in a gaseous state, making sputtering unnecessary.

LASER OPTOGALVANIC SPECTROSCOPY

The method which detects changes in the energies of atoms or molecules caused by optically induced current changes is known optogalvanic spectroscopy. It is an excellent, simple and relatively inexpensive method of performing laser spectroscopy of gas discharges. [1] A solid is plated onto the cathode of a hollow cathode lamp, which also contains an inert carrier gas, often neon at a low pressure. Current is run from the anode to the cathode and the electrical discharge results in the vaporization of the plated solid. Energy can be absorbed when a tunable laser beam passes through the discharge volume of ions or atoms if the wavelength $\lambda = hc/\Delta E$ is tuned to ΔE, the absolute value of the transition energy between the lower energy state E_1 and the excited energy state, E_2. The population densities $n_1(E_1)$ and $n_2(E_2)$ of the two states are changed by this optical pumping. The different ionization probabilities of the two levels causes a change in population and results in a change in the discharge current ΔI. This change in current is detected as a voltage change $\Delta V = R_b \Delta I$ across the ballast resistor shown in Figure 1.

If P(E) is the total ionization probability of the atom in state E, the voltage change produced by the laser induced population changes in the two states is given by:

$$\Delta V = C\,[\Delta n_1\, P(E_1) - \Delta n_2\, P(E_2)] \qquad (1)$$

where C is a constant. There are three possible mechanisms for the ionization of atoms from level E_1 to E_2:

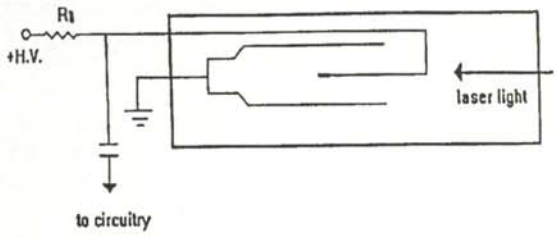

Figure 1
Schematic of an optogalvanic cell.

Doug completed this research as a senior honors project while majoring in physics. He is presently in graduate school at the University of Denver.

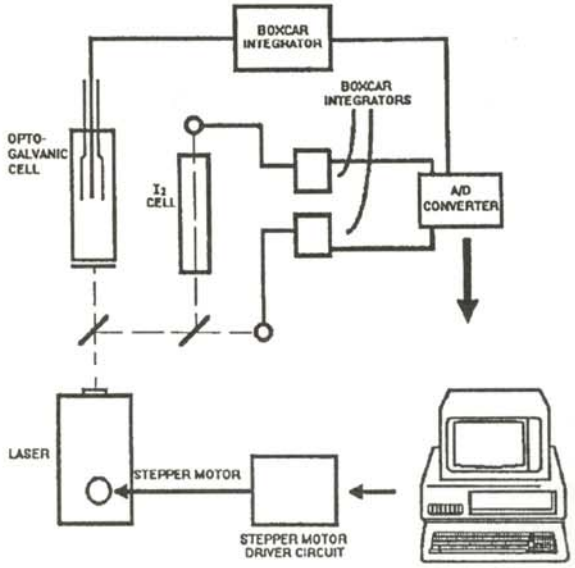

Figure 2
Schematic of the experimental set-up.

1) direct ionization by impact of an electron
$$A(E_1) + e^- \text{ --------> } A^+ + 2e^-$$
2) ionization caused by collision with a metastable atom
$$A(E_1) + A^* \text{ --------> } A^+ + A + e^-$$
3) direct photo-ionization by the laser photons
$$A(E_1) + h\nu \text{ ---------> } A^+ + e^-$$

The competition between these and other mechanisms will determine whether the population changes cause an increase or decrease in the discharge current. This determines whether a positive or negative optogalvanic signal is observed.

With moderately powerful pulsed lasers in the kilowatt range, voltage signals in the micro to millivolt range can be observed. This makes the optogalvanic effect (OGE) sensitive enough to resolve vibrational changes in molecular bonds and differences in energy levels brought about by different electron spins.

There are several limitations to optogalvanic spectroscopy. For highly sensitive experiments, Doppler shifts must be eliminated. This is usually done by using a discharge cell with an optical quality window and placing it within the laser resonating cavity, taking advantage of the amplification effects within the cavity. [1]

For our research, Doppler shifting was not a concern. The prime limiting factor in resolving the spectral lines was the laser itself. Our laser was not monochromatic enough to resolve line broadening due to the Doppler shifting of neon atoms or the rotational levels in molecules. Because of this, the current research was restricted to the study of the electronic excitations of neon.

Another limitation was the gas pressure within the cell. As the laser light shines on the sample and current is run through it, the pressure of the gas within the cell increases. This is partly due to the heating of the sample and partly due to the sputtering of the species. As the pressure within the sample increases or decreases, the impedance of the optogalvanic cell will change and appear as a signal at the output. For sputtering to occur, the pressure inside the cell has to be kept below 5 - 10 Torr.

SYSTEM COMPONENTS

A schematic layout of the experimental set-up is shown in Figure 2. The computer we chose is an IBM PC-AT compatible because it was inexpensive and it was easy to purchase standard data acquisition cards for the computer. The laser is a Chromatix CMX-4 flashlamp pumped tunable dye laser The dye we used is Rhodamine-6G which restricts the wavelength range to 563-633nm. At peak efficiency, it has an output of about 1-5 mJ/pulse with a 2μs pulse at a repetition rate of 10 Hz. A computer driven stepper motor is used to turn the tuning of the knob of the laser. Each step will change the wavelength of the laser about 0.2 nm.

The beam travels to a splitter which devides off 8%. This 8% is split again, a portion traveling to a photodiode to measure the intensity of the beam and the other portion passes through a cell containing heated iodine. Iodine has a well-known absorption spectrum with relatively evenly distributed spectral lines across the tunable range of the laser. The resulting spectral lines, detected by another photodiode, serve as convenient wavelength markers for determining the wavelength at which the laser is operating.

The light not split off by the first beam splitter passes to the optogalvanic cell. The electronic signals from it and the two photodiodes are sent to boxcar integrators. The integrators are gated by a pulse generated by the laser when it fires. The gate pulse has a slight delay and is significantly longer than the laser pulse to overlap the

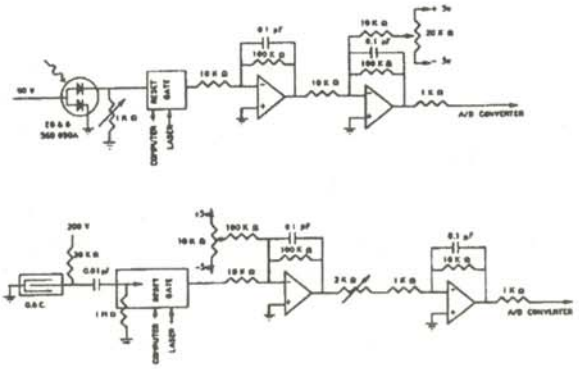

Figure 3
Schematic diagram of the analog electronics used in the experiment.

OGE signal. Since this pulse is simultaneous with the laser pulse, the integrators will receive a signal only when laser light is incident upon the cell. This procedure reduces the noise level significantly. The voltage outputs from the integrators are fed into an analog to digital converter so that they can be read by the computer.

CIRCUITRY

This section describes the circuitry that was built 'in-house'. The stepper motor driver circuit consists of a n-pulse generator [3], an SAA1027 stepper motor driver chip and 4 MOSFET transistors which drive the stepper motor. The n-pulse generator receives a single triggered pulse from the computer and outputs n pulses which the operator can set using 4 binary coded decimal switches. Each step of the stepper motor causes a fixed change in wavelength of the laser, so the operator can set how many steps the stepper motor takes for each pulse sent by the computer. The SAA1027 chip not only causes the stepper motor to take a step, but also can determine which direction the motor steps. The direction is controlled by a level set by the computer. To provide the current needed to run the stepper motor, the outputs of the SAA1027 chip are buffered by the 4 MOSFET transistors.

Figure 3 shows the signal processing for the two photodiodes. The photodiodes are biased at -90V to improve their frequency response. The optogalvanic cell is biased at 300-500V through a 20 kΩ resistor. The series capacitor in conjunction with a 1 MΩ grounding resistor in the boxcar amplifier serves to block the DC voltage and transmit only changes in voltage, in this case pulses from the optogalvanic cell. The operational amplifier which follow the boxcar integrators provide amplification as well as zero offset adjustment. This offset can be used to set the height of each display sweep as seen on the computer screen. When a pulse is received from the laser, a gate within each integrator opens and the incoming data is integrated. The computer then reads the voltage output from the integrators. When the computer sends the pulse to the stepper motor driver circuit, it is also sent to the integrator to reset the boxcar. Each time a step is taken by the driver motor, the integrator is reset and new data is collected for that step or wavelength.

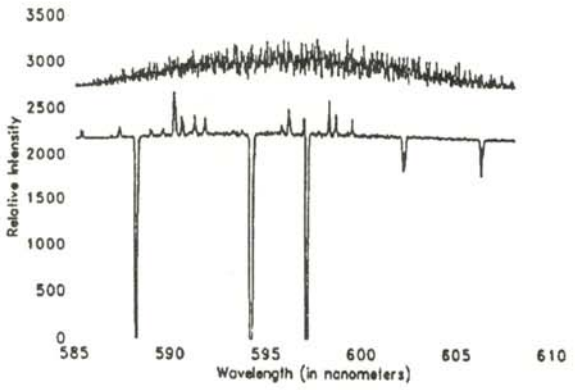

Figure 4
Typical output from our apparatus showing a neon spectrum with traces of sodium. The upper trace is the laser intensity. The lower trace is the optogalvanic spectrum.

THE COMPUTER PROGRAM

The computer program used to control the experiment and view the results was written in QuickBASIC 4.5. The program consists of about 170 modules, functions and subroutines. The main module and twenty sub-modules were written 'in-house'. The remaining routines were purchased and modified to fit our needs. A copy of the program and various routines is available from the faculty sponsor of this paper.

The program has three main functions: send a signal to the stepper motor driver circuit and boxcar integrator; receive data from the A/D converter; and store, retrieve and display output from the A/D converter. The 'ScanLaser' module is the heart of the program. It initializes the data acquisition board, collects data from all three inputs and displays them in real time. The routine that steps the stepper motor is called approximately every 2 seconds. This may seem quite rapid, but with 1500 steps to scan, one scan takes nearly an hour to complete.

DISCUSSION OF RESULTS

The assembled equipment worked extremely well. A typical result is sown in Figure 4. Both positive and negative going peaks are observed in the optogalvanic spectrum. The relative intensity is adjusted so that the peaks are full scale on the analog to digital converter used, when measured using the circuitry in Figure 3.

The identification of the lines shown in Figure 4 are shown in Table 1. We clearly identify several of the excited states of neon within 0.2% of those given in the M.I.T. wavelength table.[2] We were able, with few exceptions, to observed the close to ionization states of neon. Table 1 shows that we saw the sodium D lines. This comes from the lamp that we used. Other lamps we used contained traces of potassium, copper, calcium and lithium. However, the excited states of neon consistently dominated each of the 60 scans we took.

The iodine reference spectrum technique rarely worked. We were forced to use a monochrometer to separately calibrate the wavelength of the laser. We will need to develop a better method for wavelength calibration. The stepper motor was attached by a band to a knob which is in turn attached to the prism mounts that tune the laser by an intricate series of bands. This caused the movement of the prism to not necessarily precisely follow the turning of the knob or the stepping of the motor.

It is important to note that this research is not complete. We now know that the equipment works and we know its

M.I.T. Lambda (nm)	Our Lambda (nm)	Difference (nm)	% Diff.	Remarks
585.24878	585.2979	0.04912	0.0084	
587.2149	587.2895	0.0746	0.0127	
588.1895	588.184	0.0055	0.0009	
588.995	588.876	0.119	0.0202	Sodium
589.592	589.5342	0.0578	0.0098	Sodium
590.2464	590.1249	0.1215	0.0206	
590.6429	590.4962	0.1467	0.0248	
591.3633	591.2051	0.1582	0.0268	
591.8914	591.7114	0.18	0.0304	
594.48342	594.1755	0.30792	0.0518	
596.1626	595.6945	0.4681	0.0785	
596.5474	596.1502	0.3972	0.0666	
597.4628	596.9266	0.5362	0.0898	
597.5534	597.0616	0.4918	0.0823	
598.7907	598.243	0.5477	0.0915	
599.1675	598.5974	0.5701	0.0952	
600.0951	599.4582	0.6369	0.1062	
602.99971	602.1417	0.85801	0.1424	
607.43377	606.2936	1.14017	0.1879	

Table 1
Wavelengths of the major optogalvanic signals from neon that we detected in our experiment.

shortcomings. It is now possible to continue with the next phase of the experiment, examining those electronic states of titanium oxide and aluminum(I) fluoride near ionization.

ACKNOWLEDGMENTS

This research was funded by grants from the Petroleum Research Fund and the UNC Faculty Research and Publication Board. Dr. Richard Schwenz provided guidance and support for most aspects of this project. Dr. Robert Walch provided valuable technical support and guidance. Dr. Peter Isaacson provided suggestions on computer programming. Ken Cochran assisted by building the stepper motor mount for the laser and Andy Loomis assisted in designing and building the circuitry. Helpful suggestions from students Jennifer Frank, Greg Goodel and Tim Champion are also acknowledged.

REFERENCES

1. W. Demtröder, Laser Spectroscopy: Basic Concepts and Instrumentation, 2nd Corrected Printing, Springer-Verlag, Berlin, 1981, pp. 395-397.

2. G.R. Harrison, Wavelength Tables, M.I.T. Press, Cambridge, 1969.

3. P. Horowitz and W. Hill, The Art of Electronics, Cambridge University Press, 1989, P. 371.

FACULTY SPONSORS

Dr. Richard Schwenz, Department of Chemistry
Dr. Robert Walch, Department of Physics
University of Northern Colorado
Greeley, CO 80639

SEPARATION OF ON-AXIS SCATTERED AND UNSCATTERED LIGHT BY RED BLOOD CELLS USING POLARIZATION TECHNIQUES†

Jerry N. Sanders, Jr., Frederick J. Barrera and Babak Nemati
Division of Earth and Physical Sciences
University of Texas at San Antonio
San Antonio, TX 78285
Received September 24, 1991

ABSTRACT

This study used a polarimeter to filter out the contribution of scattered light to the net on-axis transmission of electromagnetic radiation. The light from a Ne-He laser was scattered by red blood cells (RBC). The difference in detected intensity with and without polarization filtering gave us a measure of the filtered light intensity. The scattering level was varied by altering the distance between detector and samples, using erythrocytes from three different species (dog, goat and human, which are known to have different RBC sizes) and allowing the RBC from each species to shrink and swell osmotically. The wavelength dependence of the filtered scattering intensity was determined using an Ar^+ laser. The results obtained were in close agreement with the expected contribution of scattered radiation to the net axial transmission.

INTRODUCTION

When an electromagnetic wave traverses a particulate medium, it is attenuated by the processes of absorption and scattering. In homogeneous media, the dominant attenuation mechanics is absorption, while in heterogeneous media, such as biological membranes, each mechanism plays a substantial role in the extinction process. A clear understanding of these processes in biological molecules is of substantial significance in photobiological studies. Theoretical models of the optical properties of whole blood have been instrumental in the design of practical instruments such as hemoglobinometers and oximeters.[1]

Many theoretical models have been developed to describe the propagation of electromagnetic radiation through turbid media. [2,3,4] An underlying assumption in such theoretical models is that the scattered light, regardless of the scattering angle, is excluded from the detected on-axis transmission. [5] To do this experimentally, is difficult, since all detectors collect some small solid angle around the forward direction. This assumption is incorporated in the design and construction of many optical detection systems. Most conventional spectrophotometers are not designed to reject the contribution of scattered light at small angles with respect to the on-axis transmission. Such instruments are adequate for transmission/extinction measurements involving scattering particles that have dimensions that are much smaller than the wavelength of the incident radiation. When the scattering particles are larger, however, the attenuation of the light in the medium is dominated by Mie scattering, and the forward-scattered light substantially influences the on-axis transmission. [6]

One solution to this problem is to collimate the incident radiation, focus the light that is transmitted through the medium on a pinhole and measure the intensity of the light that is transmitted through the aperture. While this method overcomes the existing problem, the alignment, aberration of the lenses and the positioning of the optical components could pose experimental problems in the construction of spectrophotometers.

A more effective and practical solution to this problem is to use polarized light. The incident beam is polarized before it traverses the turbid medium. The transmitted beam is analyzed with a polarizer with a parallel orientation. The portion of the light that is scattered by the medium changes its polarization and consequently is blocked by the polarizer in the transmitted beam. The difference between the intensity of the scattered light with and without the polarization filtering gives us a measure of the portion of the detected on-axis signal that was due to scattering.

Jerry is a senior majoring in physics. After completing his B.Sc., he plans to pursue a Ph.D. in medical physics. Fred is a physics major and plans to pursue graduate study in physics. Babak has earned a B.Sc. in physics from the University of Texas at Austin and is currently a graduate student in the Department of Biomedical Engineering. This project came out of a summer research program sponsored by the NSF-REU at UTSA.

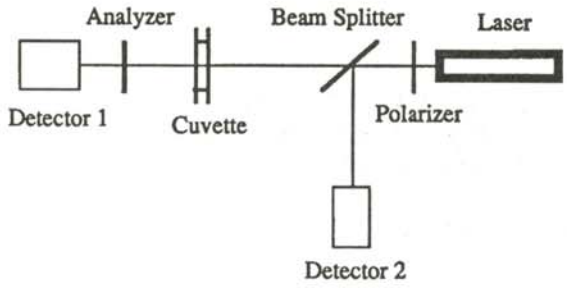

Figure 1
Schematic view of the experimental set-up.

THEORETICAL BACKGROUND

Scattering is primarily the process of an elastic interaction between radiation and the scattering medium in which only the direction of propagation of the photon is altered. Scattering effects are direct consequences of physical inhomogeneities in the medium. The spatial distribution and intensity of scattered light depend upon the size and shape of the scattering centers relative to the wavelength of the incident radiation and the difference in refractive index between the medium and the scattering elements.

One of the basic models used to study the attenuation of light in turbid media is the Lambert-Beer law:

$$T_c = \exp[-(\Sigma_s + \Sigma_a)\, d], \qquad (1)$$

where T_c is the collimated transmittance, Σ_s is the macroscopic scattering coefficient, Σ_a is the macroscopic absorption coefficient and d is the optical path length. When this model is applied to extinction studies in whole blood, the macroscopic scattering coefficients can be approximated by [7].

$$\Sigma_s = H\, \sigma_s\, (1 - H) / V$$
$$\Sigma_a = H\, \sigma_a / V, \qquad (2)$$

where H is the hematocrit (the fractional volume of the red blood cells (RBC) in whole blood after centrifugation, ranging from 0 to 1), V is the volume of a single RBC, and σ_s and σ_a are the microscopic scattering and absorption cross sections. H/V then represents the density of scattering elements. In low hematocrit samples, the macroscopic scattering coefficients are proportional to the density of scatterings with the microscopic cross sections as the constants of proportionality.

Since the wavelength of the He-Ne laser is between 400 and 625 times larger than the microscopic absorption cross section[7,8], we can approximate Equation 1 as:

$$T_c \approx \exp\,(-\Sigma_s\, d)\,. \qquad (3)$$

As H approaches 0, we can substitute an approximation of Equation 2 into Equation 3 to get:

$$T_c \approx \exp[-(H/V)\, \sigma_s\, d] \qquad (4)$$

The optical density of the sample, $O.D._{col}$ can be found by taking the log of $1/T_c$, so Equation 4 can be rewritten as:

$$OD._{col} \approx H/V\, \sigma_s\, d\,. \qquad (5)$$

PREPARATION OF SUSPENSIONS

The procedure used to extract and prepare the red blood cell suspension followed the steps outlined in an earlier study of the scattering properties of RBC.[1] The blood was obtained by performing venipuncture to withdraw approximately 20 ml of blood from males of three species (goat, dog and human) that are known to have red blood cells of different sizes. 1000 units of Heparin were added to the samples to prevent coagulation. The samples were then centrifuged at high speed for approximately 10 minutes to separate the RBC. The aliquots were then centrifuged to give a hematocrit of packed RBC. Small volumes of the packed RBC were then re-suspended in a hypertonic solution of 1.5% NaCl, an isotonic solution of 0.9% NaCl and a hypotonic solution of 0.5% NaCl. The suspension in the hypertonic and hypotonic saline solutions allowed the RBC to osmotically shrink and swell respectively, thereby altering the dimensions of the scattering elements in the medium. The smaller goat RBC, however, did not survive the osmotic swelling in 0.5% saline solution and complete hemolysis occurred. The human and canine RBC were performed successfully as no hemolysis occurred.

The blood plasma of the different species have different indices of refraction due to the difference in protein concentration. Suspension of the RBC in NaCl had the added advantage of eliminating the refractive index of the plasma as an uncontrolled variable. We shook the samples in room air to provide a high level of oxygenation of the RBC suspensions. All measurements were made on the same day that the blood was drawn and within 2 minutes after the sample was placed in the cuvette.

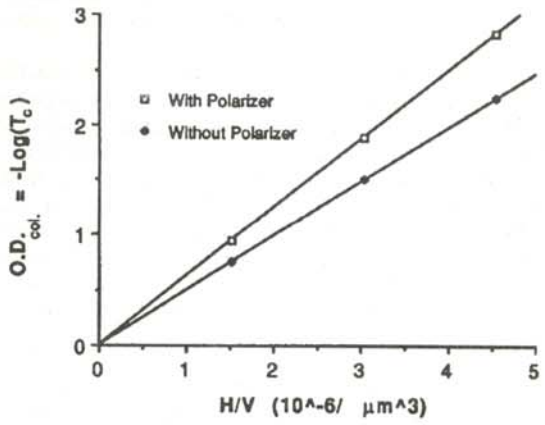

Figure 2
Logarithm of the collimated transmittance ($O.D._{col} = -\log_{10}T_c$) vs. the hematocrit-to-cell volume ratio (H/V). Data are from the canine RBC suspended in 0.9% saline solution (isotonic). The line is a fit through the origin. The detector-sample separation was 11.6 cm.

EXPERIMENTAL SETUP

Figure 1 is a schematic of the experimental setup used in this study. A 7 mW He-Ne laser [9] was used as the primary source of the radiation because its spectral region is of interest to the studies in oximetry and hemoglobinometery. An Ar^+ laser [10], whose 5 W beam was attenuated to 100 mW before it was passed through the sample, was used to provide a source of electromagnetic waves of a different wavelength. The light beam initially passed through a polarizing film and then passed through the sample contained in a thin (140 μm) cuvette. Finally, the beam passed through an analyzer that was fixed at parallel position with respect to the first polarizer.

Earlier studies on the polarization properties of the He-Ne laser showed that in a multi-mode low powered laser with internal mirrors, the signal can fluctuate dramatically after it traverses a polarizing element due to mode competition within the cavity as well as polarization flips. [11] To overcome this problem we devised a normalized detector[12] where we measured the intensity of the beam before it entered the sample as well as after it traversed the analyzer. The latter reading was then normalized with respect to the first reading.

EXPERIMENTAL PROCEDURE

The absence of a contribution of scattered light in the detected signal means that this signal is smaller when it is filtered,hence the optical density (see Equation 5) obtained with polarization filtering is larger. Figure 2 is a graph of optical density vs H/V, the concentration of RBC for canine blood cells suspended in 0.9% saline solution. The squares represent data obtained with the polarizer and the diamonds represent data taken without the polarizer. The straight lines and smaller slope of the filtered data verify Equation 5.

To help verify that we were indeed only eliminating scattered radiation we altered the distance between the sample and the detector. Figure 3 shows the correlation between the measure of filtered scattered light and the sample-detector separation. As the detector-sample separation increases, the scattered light diverges while the unscattered

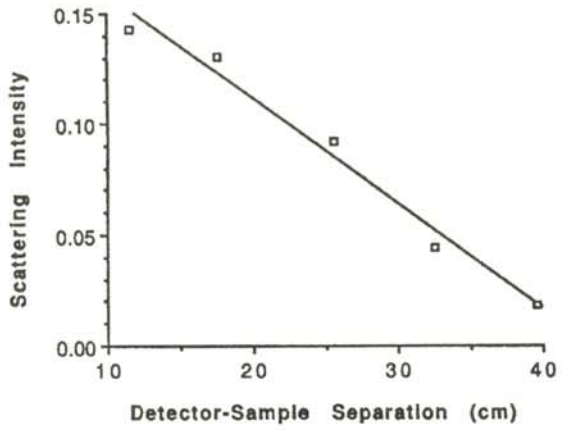

Figure 3
Normalized scattered light intensity vs. detector-sample separation for canine erythrocytes. The suspension was 2% hematocrit in isotonic (0.9% saline) solution.

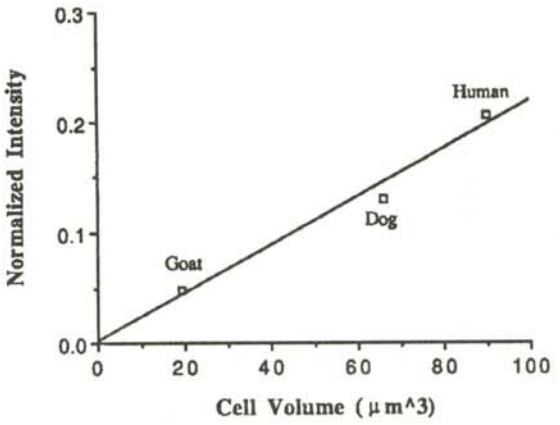

Figure 4
Normalized scattered light intensity vs. cell volume of erythrocytes from the three species. The RBC's were suspended in an isotonic solution. The detector-sample separation was 17.6 cm.

light contribution should remain constant, causing the filtered light intensity to drop with detector-sample separation.

Figure 4 shows our results when the cell volume changes. Our results show that the scattering is directly proportional to cell volume and would fall to zero if the volume were zero. To verify this, we used osmotically shrunken and swollen RBC. Figure 5 shows a positive correlation between the osmotically varied sizes of the RBC and the level of filtered scattered radiation. As the percent NaCl in solution increases, the cell size shrinks. This shows that the microscopic scattering cross section varies directly with the cell size.

The relationship between the level of on-axis scattered light intensity and the wavelength of the incident visible radiation is shown in Figure 6. The scattering decreases

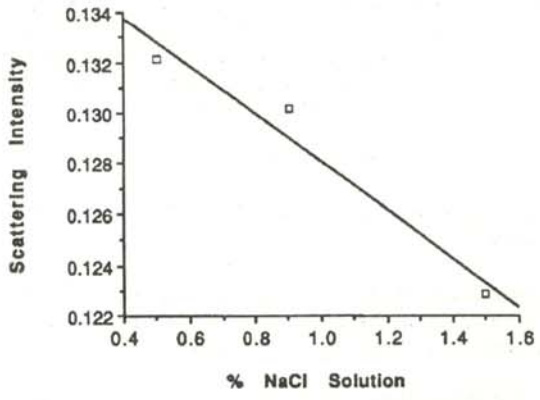

Figure 5
Normalized scattered light intensity vs. percent saline solution for canine red blood cells. The data were taken with 2% hematocrit. Detector-sample separation was 17.6 cm.

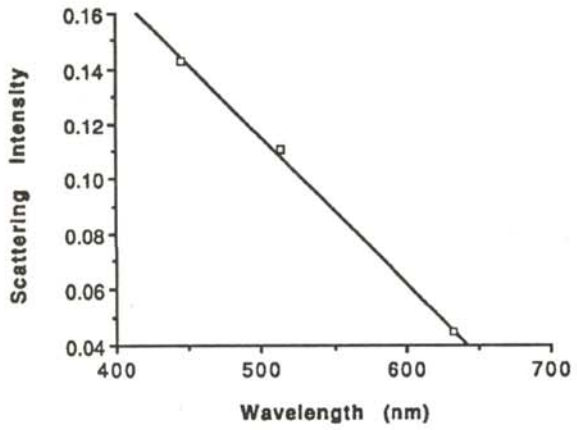

Figure 6
Normalized scattered light intensity vs. the laser wavelength. The suspension was 2% hematocrit from the canine RBC suspended in isotonic (0.9% saline) solution. The detector-sample separation was 25 cm.

with the increase in wavelength. With the Ar^+ light, the RBC's are larger than the incident wavelength and the scattering is therefore dominated by Mie scattering where the forward scattered light substantially influences the on-axis transmission.

The close agreement of the variation in the measure of forward scattered radiation with the expected behavior verifies the effectiveness and validity of our method. Our study, therefore, suggests that the use of polarization techniques for separating the on-axis scattered light in turbid media (such as biological tissue) can be implemented in spectrometric measurements.

ACKNOWLEDGMENTS

The authors are indebted to Dr. Dhiraj Sardar for his continuous support and encouragement during this research project. We would like to thank Cheryl Burns and Robyn Miller of the University of Texas health Science Center for their assistance in the extraction and preparation of the blood samples. We would also like to extend our thanks to Dr. Andrew Martinez and Linda Armstrong of the University of Texas at San Antonio for letting use their Ar^+ laser and for their technical assistance.

REFERENCES

† This research was supported by NSF grant DMR 8900834.

1. J.M. Steinke and A.P. Shepherd, *Comparison of Mie Theory and the Light Scattering of Red Blood Cells*, J. Opt. Soc. Am., 27, 1988, pp. 4027 - 4033.

2. P. Kubelka, *New Contributions to the Optics of Intensely Light-Scattering Materials, Part 1.*, J. Opt. Soc. Am., 38, 1948, pp. 448 - 457.

3. S. Chandrasekhar, Radiative Transfer, University Press, London, 1960.

4. A. Ishimaru, Wave Propagation and Scattering in Random Media, Vol. 1, Academic Press, New York, 1978.

5. C.F. Bohren and R.R. Huffman, Absorption and Scattering of Light by Small Patricles, John Wiley & Sons, New York, 1983, p. 316.

6. As the dimensions of the light-scatterers increase (relative to the wavelength), the scattering becomes more forward-directed. In the case of scattering particles that are far larger than the wavelength, the scattering is called Mie scattering, in which case it is weak and highly forward-directed.

7. J. M. Schmitt, *Optical Measurement of Blood Oxygen by Implantable Telemetry*, Ph.D. Dissertation, Stanford University, 1986.

8. L.O. Reynolds, *Optical Diffuse Reflectance and Transmittance From an Anisotropically Scattering Finite Blood Medium*, Ph.D. Dissertation, University of Washington, 1975.

9. Uniphase Model 105-1. Beam diameter 0.83 mm at $1.e^2$.

10. Specta-Physics Model 2025, Series 2000. Beam diameter 1.25 mm at $1.e^2$.

11. E.K. Hasle, *Polarization Properties of He-Ne Lasers*, Optics Commun., 31, 1979, pp. 206 - 210.

12. The detectors used were United Technology type PIN-6DP.

FACULTY SPONSOR

Dr. Dhiraj Sardar
College of Sciences and Engineering
Division of Earth and Physical Sciences
The University of Texas at San Antonio
6900 North Loop 1064 West
San Antonio, TX 78249-0663

The Journal of Undergraduate Research in Physics

The **Journal of Undergraduate Research in Physics** is the journal of Sigma Pi Sigma and the Society of Physics Students. It is published by the Physics Department of Guilford College, Greensboro NC 27410. Inquiries about the journal should be sent to the editorial office.

The Journal of Undergraduate Research in Physics

Editorial Office -
The Journal of Undergraduate Research in Physics
Physics Department
Guilford College
Greensboro, NC 27410
919-316-2279 (voice)
919-316-2951 (FAX)

Editor -

Dr. Rexford E. Adelberger
Professor of Physics
Department of Physics
Guilford College
Greensboro, NC 27410
ADELBERGERRE@RASCAL.GUILFORD.EDU

The Society of Physics Students

National Office -
Dr. Donald Kirwin, Executive Director
Dr. Edwin Goldin, Associate Director
Society of Physics Students
American Institute of Physics
1825 Connecticut Avenue, N.W.
Suite 213
Washington, DC 20009
202-232-6688

President of the Society -
Dr. Jean Kirsch
Department of Physics
University of Michigan

President of Sigma Pi Sigma -
Dr. Reuben James
Department of Physics
SUNY College at Oneonta